Geological Magazine

www.cambridge.org/geo

Original Article

Cite this article: Kwayisi D, Amponsah PO, Agra NA, Nunoo S, Thompson J, Kazapoe RW, Anani CY, Asiedu D, and Nude PM. Neoproterozoic passive margin formation and evolution during the Rodinia–Gondwana supercontinent cycle at the eastern margin of the West African Craton. *Geological Magazine* **161**(e14): 1–23. https://doi.org/10.1017/S001675682400027X

Received: 17 March 2024
Revised: 26 August 2024
Accepted: 8 September 2024

Keywords:
Passive margin; Togo Structural Unit (TSU); geochemical data; Dahomeyide belt; Pan-African orogeny; Rodina–Gondwana supercontinent

Corresponding author:
Prince Ofori. Amponsah;
Email: pamponsah@ug.edu.gh

Neoproterozoic passive margin formation and evolution during the Rodinia–Gondwana supercontinent cycle at the eastern margin of the West African Craton

Daniel Kwayisi[1,2], Prince Ofori Amponsah[2], Naa Afi Agra[2], Samuel Nunoo[2], Joseph Thompson [2], Raymond Webrah Kazapoe[3], Chris Yao Anani[2], Daniel Asiedu[2] and Prosper M. Nude[2]

[1]Department of Geology, University of Johannesburg, Auckland Park Kingsway Campus, Johannesburg, South Africa; [2]Department of Earth Science, University of Ghana, Accra, Ghana and [3]Department of Geological Engineering, University for Development Studies, Nyankpala, Ghana

Abstract

Petrographical and geochemical data from the Togo structural unit (TSU), also referred to as the Atacora structural unit, are presented together with the existing dataset; geochemical and age data from the sedimentary and metasedimentary rocks from the passive margin sequences of the Dahomeyide belt in Ghana to infer their provenance and depositional setting and expand the discussion on the Rodina–Gondwana supercontinent assembly during the Pan-African orogeny. The metasedimentary rocks of the TSU are quartzites and phyllites. The framework grains of the quartzites consisting dominantly of quartz and small amounts of feldspar grains and relict lithic fragments classify them as quartz arenite, subarkose and sublitharenite. Generally, the studied rocks show similar rare-earth element and multi-element patterns, which imply derivation from similar sources. Elemental ratios, including $(La/Lu)_N$, Th/Sc and La/Sc, suggest sediments sourced from intermediate to felsic rocks. Provenance and depositional setting indicators of the TSU suggest deposition in a passive margin setting, with the West African and Amazonian cratons' granitoids and granitic gneisses as possible provenance, akin to siliciclastic rocks of the Buem structural unit and the Voltaian Supergroup of the Volta Basin. The deformational history of the TSU is similar to those of the Buem structural unit and the eastern margin of the Voltaian Supergroup, indicating the effect of the Pan-African orogeny on the passive margin of the Dahomeyide belt. We, therefore, propose the formation and evolution of a Neoproterozoic passive margin unit, which was tectonically deformed during the Rodinia–Gondwana supercontinent cycle.

1. Introduction

The tectonic setting, proto-source rock composition, paleoclimatic and paleoweathering conditions of siliciclastic sedimentary rocks are all revealed by the petrographic and geochemical data of these rocks (Bhatia & Taylor, 1981; Dickinson, 1985; Verma & Armstrong-Altrin, 2016). The major and trace element compositions of siliciclastic rocks manifest the composition of the source rocks since certain trace elements, like the rare-earth elements (REEs) and high-field strength elements (HFSE), are usually not mobile during weathering and transportation and stay as solid (particulate) load, i.e., reflecting the source composition (Bhatia & Taylor, 1981; Verma & Armstrong-Altrin, 2016). When eroded, unique siliciclastic sedimentary rocks with distinctive mineralogical compositions and textural features are produced because different tectonic settings are defined by different rock types (Dickinson, 1985). The youngest zircon age population in siliciclastic sedimentary rocks can be used to infer the maximum age of deposition of the sediments into the sedimentary basin (Fedo *et al.*, 2003; Yao *et al.*, 2011). History of crustal growth and evolution, correlations of continental blocks within supercontinents and reconstruction of palaeogeography of geological terranes can be constrained from detrital zircon ages of sedimentary basins (Yao *et al.*, 2011; Cawood *et al.*, 2012; Andersen *et al.*, 2016). Combining petrography and whole-rock geochemical data together with detrital U-Pb zircon ages, the provenance of siliciclastic sedimentary rocks in several basins and their depositional setting have been inferred (Anani *et al.*, 2017, 2019; Baiyegunhi *et al.*, 2017; Jiang *et al.*, 2017; Kwayisi *et al.*, 2022b).

The Dahomeyide belt is a Neoproterozoic orogenic belt that forms a part of the West Gondwana Orogen at the south-eastern margin of the West African Craton (WAC) (Fig. 1a and 1b, e.g., Attoh, 1998; Attoh & Nude, 2008; Kwayisi *et al.*, 2020). The Dahomeyide belt consists of key features of

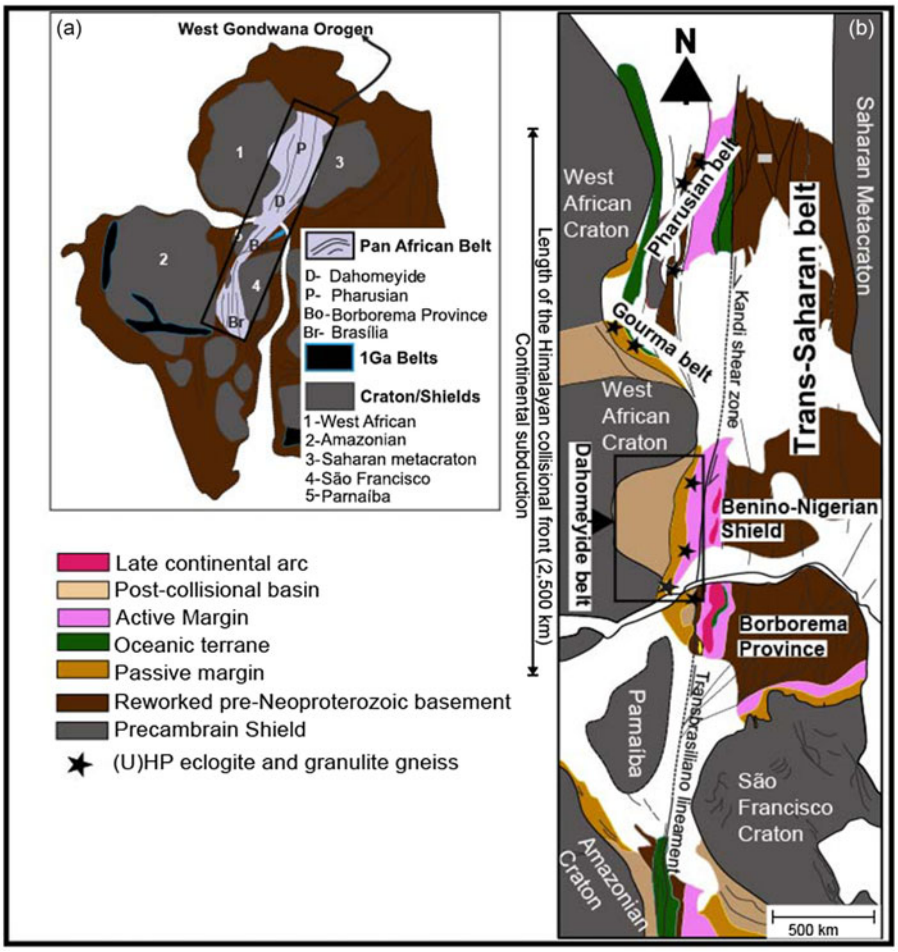

Figure 1. (a) A schematic map of Africa and South America showing the various cratons and Pan-African orogenic belts and (b) geological map of West Gondwana orogen (modified after Kwayisi *et al.*, 2022a).

typical collisional belts such as passive margin sequences, oceanic terrane, active margin (i.e. arc crust), post-collisional basins and basement complexes (Fig 1b; Ganade de Araujo *et al.*, 2014a; Kwayisi *et al.*, 2020). This Dahomeyide belt stretches 1000 km N-S and 400 E-W from Ghana, Togo and Benin to Nigeria (Agbossoumonde *et al.*, 2001; Attoh & Nude, 2008; Nude *et al.*, 2015). Three main nappes zones comprise the Dahomeyide belt, and these are (i) internal nappes zone, (ii) suture zone and (iii) external nappes zone (Attoh and Nude, 2008; Nude *et al.*, 2015; Aidoo *et al.*, 2020; Kwayisi *et al.*, 2022a). Occurring in the external nappes zone of the Dahomeyide belt are siliciclastic rocks of the Buem structural unit and Togo structural unit (TSU) (Osae *et al.*, 2006; Attoh & Nude, 2008; Kwayisi *et al.*, 2020, 2022b), also known as the Atacora structural unit (Affaton *et al.*, 1997; Alayi *et al.*, 2023) of foreland and passive margin affinities evident from geochemical and geochronological data (Kalsbeek *et al.*, 2008; Ganade de Araujo *et al.*, 2016; Kwayisi *et al.*, 2022b). The Amazonian Craton, Benin-Nigerian Shield, ± West African Craton have been proposed as the possible sources of sediments for these sequences (Kalsbeek *et al.*, 2008; Ganade de Araujo *et al.*, 2016; Anani *et al.*, 2019; Kwayisi *et al.*, 2022b). Kalsbeek *et al.* (2008) and Kwayisi *et al.* (2022b) indicated that passive margin formation may have been deposited *c.* 1000 – 700 Ma. In contrast, the deposition of foreland sequences occurred between 620 and 570 Ma, according to Ganade de Araujo *et al.* (2016). The youngest detrital zircon for passive margin sequences is at 900 Ma, whereas that for foreland sequences is at 600 Ma (Ganade de Araujo *et al.*, 2016; Kwayisi *et al.*, 2022b).

The TSU, which predominantly consisted of sandstones and shales, is now metamorphosed into quartzites, phyllites and schists (Kalsbeek *et al.*, 2008; Ganade de Araujo *et al.*, 2016; Anani *et al.*, 2019). The geochemical characteristics of the phyllites are akin to passive margin sequences of the external nappes zone of the Dahomeyide belt (Anani *et al.*, 2019). A passive margin setting of deposition was proposed for the TSU because of the 2200 – 930 Ma ages (U-Pb detrital zircon obtained for the quartzite (Kalsbeek *et al.*, 2008). In addition, Ganade de Araujo *et al.* (2016), based on a zircon age population between 900 and 600 Ma (U-Pb detrital zircon) from the schist, inferred a foreland basin. The available zircon U-Pb populations for the TSU are comparable to the siliciclastic rocks of the external nappes zone of the Dahomeyide belt and the Borborema Province in Brazil (Kwayisi *et al.*, 2022b). Nonetheless, no published petrographical and geochemical data are available on the quartzites and schists of the TSU to infer their depositional setting. Thus, petrography, major and trace element data of quartzites, together with new major and trace element data of the phyllites from the TSU, are presented in this study to discuss their provenance and depositional setting. The results of this study are compared to available petrographical, geochemical and geochronological data from the passive margin units of the Dahomeyide belt (i.e., Buem structural unit and the Voltaian Supergroup of the Volta Basin) to provide constraints for the development of passive margin basins and their evolution during the Pan-African orogeny and expand the discussion on the

https://doi.org/10.1017/S001675682400027X

position of West African–Amazonian cratons in supercontinent Rodina break-up and West Gondwana assembly.

1.a. Geological setting and previous work

Occurring at the eastern margin of the WAC is the Neoproterozoic Dahomeyide belt formed during the Pan-African orogeny (Attoh & Nude, 2008; Aidoo *et al.*, 2020; Kwayisi *et al.*, 2022a; 2022b). The WAC consists of a western Archean basement comprising granitoid-greenstone belts of ages between 3500 and 2500 Ma, and an eastern Paleoproterozoic Birimian domain also of granitoid-greenstone belts with ages in the range of 2200 - 1800 Ma (e.g. Kouamelan *et al.*, 1997; Potrel *et al.*, 1998; Egal *et al.*, 2002; Thiéblemont *et al.*, 2004; Sakyi *et al.*, 2014, 2018; 2020; Anum *et al.*, 2015; Grenholm *et al.*, 2019; Nunoo *et al.*, 2022; Kazapoe *et al.*, 2022; Amponsah *et al.*, 2023). Associated with the granitoid-greenstone belts are metasedimentary basins of Paleoproterozoic age (Asiedu *et al.*, 2017; Sakyi *et al.*, 2019; Kazapoe *et al.*, 2023). In most of the Rodinia supercontinent reconstruction (1000 – 1200 Ma), the Amazonian Craton is located near the WAC (e.g. Evans, 2009, 2013). Three main Archean blocks, dated at 3300 – 2600 Ma, were stabilized around 2100 Ma during the Transamazonian orogeny (2180 – 1950 Ma), which is the time equivalent to the Ebunean orogeny in the WAC (Ledru *et al.*, 1994; Tassinari *et al.*, 2001; Lofan *et al.*, 2003; Cordani *et al.*, 2009). Occurring abundantly on the Amazonian Craton in contrast to the WAC are granitoid and granitoid gneisses of late Paleoproterozoic and Mesoproterozoic (1700 – 1000 Ma) ages (Tassinari *et al.*, 2000; Santos *et al.*, 2008; Cordani *et al.*, 2009).

As stated earlier, the Dahomeyide belt consists of three main zones. These are (i) the external nappes zone, (ii) internal nappes zone and (iii) a well-defined suture zone (Fig. 2; Affaton *et al.*, 2000; Attoh & Nude, 2008). The Benino-Nigerian Shield's Paleoproterozoic (2190 – 2140 Ma, U-Pb zircon ages; Attoh *et al.*, 2013; Kalsbeek *et al.*, 2020) granitoids and gneisses comprise the internal nappes zone and are intruded by juvenile magmatic arcs and post-collisional plutons at ages of 670 – 610 Ma (Attoh *et al.*, 2013) and 580 – 540 Ma (Kalsbeek *et al.*, 2012; Alayi *et al.*, 2023), respectively. The Dahomeyide belt's upper plate and active margin (i.e. the internal nappes zone) experienced widespread migmatization and granitoid intrusion during mid-Cryogenian to early-Ediacaran (Fig. 2; Kwayisi *et al.*, 2023). A well-defined suture zone of high-pressure metamorphic rocks, including eclogite and granulite, can be found west of the internal nappes zone (Attoh, 1998; Agbossoumonde *et al.*, 2004; Attoh & Morgan, 2004; Duclaux *et al.*, 2006; Guillot *et al.*, 2019). Peak metamorphism was recorded at 610 Ma (U-Pb zircon dates; Attoh *et al.*, 1991; Affaton *et al.*, 2000). The end of collision is marked by the exhumation of the high-pressure rocks at 600 – 580 Ma (U-Pb zircon age; Attoh *et al.*, 1997).

The basement Ho-gneisses and passive and foreland sequences of the Buem – TSUs with their lateral equivalence, the Voltaian Supergroup, make up the Dahomeyide belt's external nappes zone (Kalsbeek *et al.*, 2008; Aidoo *et al.*, 2014; Kwayisi *et al.*, 2022b). Evidence from airborne geophysical and structural interpretations, as well as tectonic windows of Paleoproterozoic gneisses within the TSU, suggest the underthrust deformed WAC crust as the basement rocks of the external nappes zone (Kwayisi *et al.*, 2020; Aidoo *et al.*, 2020). The Voltaian Supergroup, which occupies the Volta Basin, is stratigraphically divided into three groups (Agyei-Doudu *et al.*, 2009). At the base is the Kwahu-Bombouaka, followed upwards by the Oti-Pendjari, with the Tamale-Obosom at the top of the supergroup (Fig. 3; Table 1; Deynoux *et al.*, 2006; Agyei-Doudu *et al.*, 2009; Kwayisi *et al.*, 2022b). Different periods of deposition in two main depositional settings have been proposed for the Voltaian Supergroup from available petrographical, geochemical and geochronological data (Table 1; Kwayisi *et al.*, 2022b). Deposition in a passive margin basin has been proposed for the Kwahu-Bombouaka Group at 959 ± 62 Ma based on Rb-Sr dating on clay minerals (Clauer, 1976; Carney *et al.*, 2010; Anani *et al.*, 2017). The Oti-Pendjari and Tamale-Obosom groups were deposited in a foreland basin setting, although the lower part of the Oti-Pendjari Group shows passive margin signatures (Table 1; Amedjoe *et al.*, 2018). The depositional age of the Oti-Pendjari Group is between 635 and 576 Ma (Barford *et al.*, 2004; Potter *et al.*, 2004); however, that for the Tamale-Obosom Group is unknown.

Kwayisi *et al.* (2020; 2022b) indicated that the lower part of the Buem structural unit consists of siliciclastic sedimentary rocks made up of meta-sandstones and shales that progress upwards to exhumed mantle peridotites, mafic plutonic and volcanic rocks and chert/jasper, with the upper part being siliciclastic sedimentary rocks. Field structural studies and airborne geophysical data interpretation have identified three main deformation events (D1 – D3) in the Buem structural unit (Kwayisi *et al.*, 2020). The most widespread is D2, which affected all the rocks. It is characterized by NNW-SSE-striking S2 foliations and F2 isoclinal and chevron folds with an E-dipping axial plane. It also contains L2 downdip stretching lineation. According to Kwayisi *et al.* (2020), D2 can be observed in the rocks of the TSU and Kwahu-Bombouaka Group. This was a result of the E-W shortening during the Pan-African subduction-collision events between 620 and 605 Ma. Three groups of siliciclastic sedimentary rocks with U-Pb detrital zircon populations of 2300–1800 Ma, 1700–1100 Ma and 1000–970 Ma exist in the Buem structural unit and are interpreted to suggest passive margin sequences from two potential sources; the Amazonian and West African cratons (Table 1; Kalsbeek *et al.*, 2008; Kwayisi *et al.*, 2022b).

The TSU occur to the east of the Buem structural unit with a tectonic contact and overlies the Ho-gneisses. It stretches from the Ghanaian coast in the southeast, through Togo to Benin, approximately 1000 km long and 10 – 50 km wide (Adjei & Tetteh, 1997; Affaton *et al.*, 1997; Figs. 2 and 3). Quartzites, phylites and schists are the principal units of the TSU (Fig. 3; Table 1; Adjei & Tetteh, 1997). Locally, small occurrences of chert, jasper and serpentinite also occur (Junner, 1935). Rocks typically strike N-S in the northern portion of the TSU, whereas a NE-SW strike is recorded for those in the southern portion (Attoh *et al.*, 1997). Adjei and Tetteh (1997) have identified three different types of folds. These folds are isoclinal, open and recumbent, of which isoclinal is widespread, similar to the Buem structural unit and the eastern margin of the Voltaian Supergroup (Kesse, 1985; Kwayisi *et al.*, 2020). Two metamorphic conditions have been reported for the TSUs, and these are upper greenschist facies at the western portion and lower amphibolite at the eastern portion (Wright *et al.*, 1985; Attoh *et al.*, 2007). Ages obtained for the TSU increase northwards with younger ages of 579.4 ± 0.8 Ma ($^{40}Ar/^{40}Ar$ studies of muscovite in the quartzite in southern Ghana), while in the north that is, Togo and Benin republics older ages of 608.1 ± 0.2 Ma have been recorded (Attoh *et al.*, 1997). The 608.1 ± 0.2 Ma age corresponds to the formation of the N-S fabrics due to an E-W shortening, whereas the 579.4 ± 0.8 Ma age corresponds to a later NW-SE thrust to produce the NE-SW fabrics (Attoh *et al.*, 1997).

Mineralogical and geochemical studies of the phyllites indicate a passive margin setting of deposition as compared to the siliciclastic rocks of the Buem structural unit and lower Voltaian

https://doi.org/10.1017/S001675682400027X

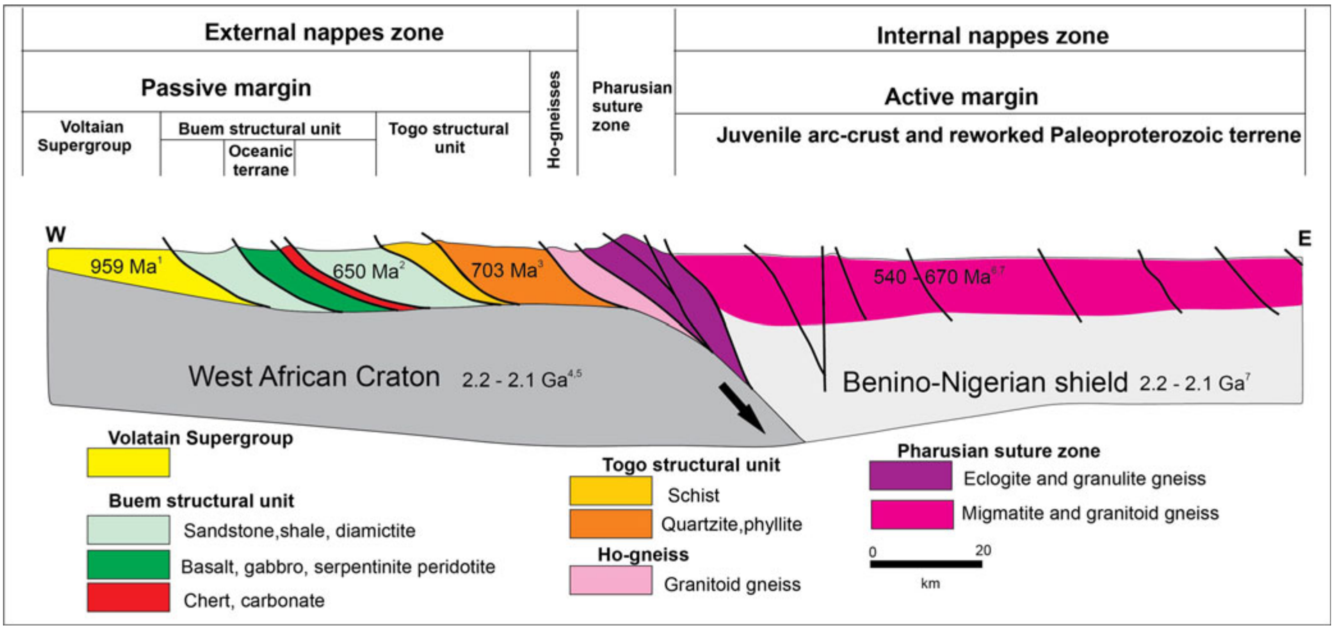

Figure 2. Schematic cross-section of the Dahomeyide belt from west to east showing the relationship between the external nappes, suture and internal nappes zones (modified after Kwayisi *et al.*, 2022b). [1]Clauer (1976); [2]Clauer *et al.* (1982); [3]Ganade de Araujo *et al.* (2014a); [4]Sakyi *et al.* (2014); [5]Amponsah *et al.* (2023); [6]Kalsbeek *et al.* (2012); [7]Attoh *et al.* (2013).

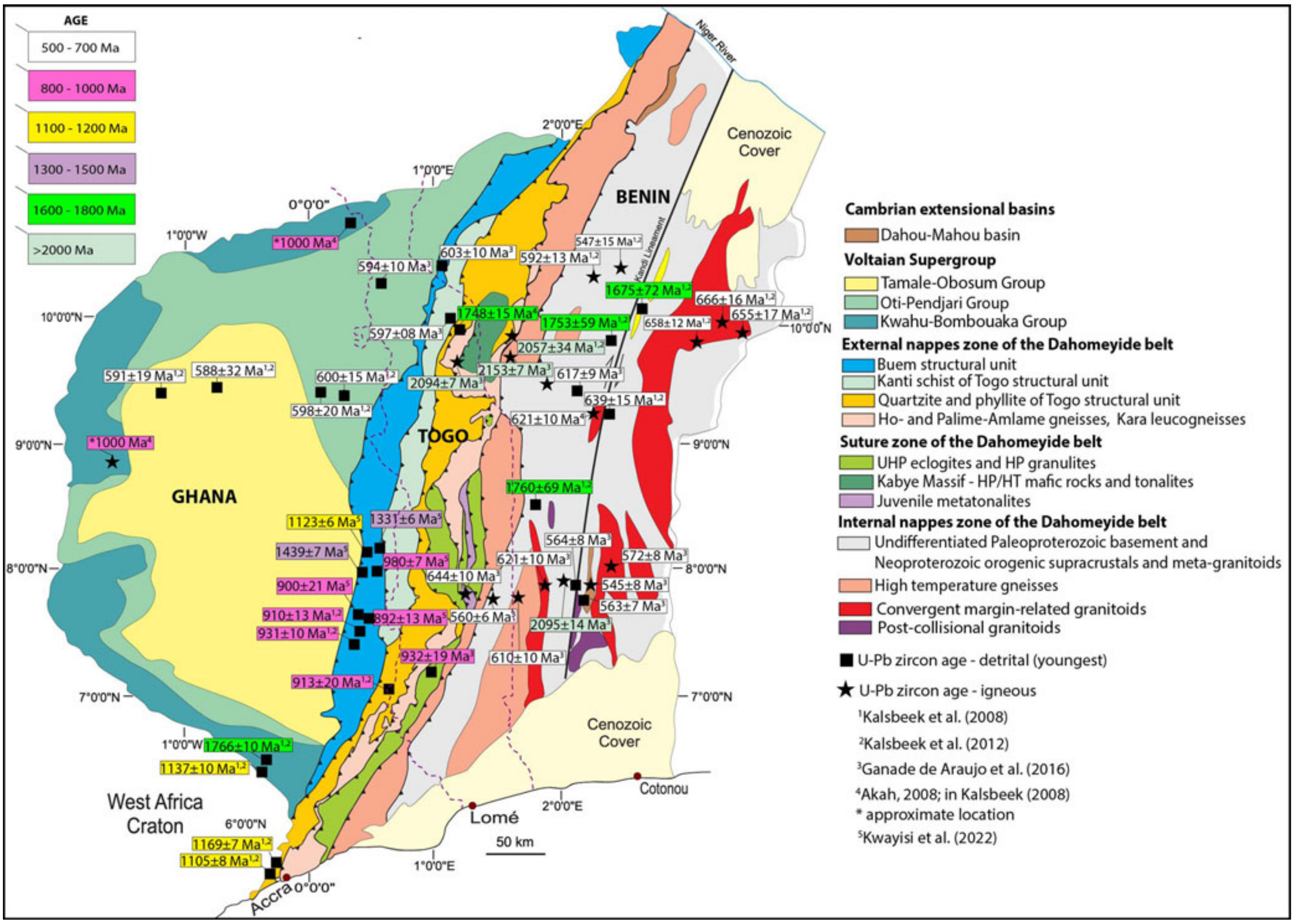

Figure 3. Geological map of the Dahomeyide belt, showing the lithological distribution of the Buem and TSUs and their relationship to the Voltaian Supergroup of the Volta Basin (Modified after Ganade de Araujo *et al.*, 2016).

Table 1. A summary of data pattern across the external nappes zone of the Dahomeyide belt (modified after Kwayisi *et al.*, 2022b)

Unit			Deposit type	Youngest zircon U-Pb age	Depositional age	Provenance
Voltaian Supergroup	Tamale-Obosum Group	Kebia Formation	Foreland (Molasse-type)[1,2]	591 Ma[1]	?	BNS[1,2]
		Yendi Formation				
	Oti-Pendjari Group	Afram-Bimbila Formation	Foreland (Flysch-type)[2,3]	600 Ma[2,3]	576 ± 13 Ma[4] (Lu/Hf, phosphorite)	BNS[3]
		Kojari-Buipe Formation	Passive margin[2,5]		*c.* 635 Ma[2] (constrained by U-Pb zircon age of Marinoan glaciation event)	WAC[5]
						Amazonian Craton and WAC[1]
	Kwaku-Bombouaka Group		Passive margin [1,2,3,6,7,8]	1100 Ma[1]	959 ± 62 Ma[9] (Rb/Sr, clay fractions)	WAC[6,7]
						Amazonian Craton and WAC[1,8]
Buem structural unit	Uppermost		Foreland[3]	600 Ma[3]	*c.* 650 Ma[12] (Rb/Sr, glauconite)	BNS[3]
	Upper and lower		Passive margin [1,3,10,11]	970 Ma[1,11]		WAC[10]
						Amazonian Craton and WAC[1,11]
Togo structural unit or Atacora structural unit	Kanti schist		Foreland[3]	600 Ma[3]	703 ± 8 Ma[14] (U-Pb zircon, metabasaltic rock)	BNS[3]
	Quartzite and phyllite		Passive margin[1,3,13]	950 Ma[1,3]		Amazonian Craton and WAC[2,13]

[1]Kalsbeek *et al.* (2008), [2]Carney *et al.* (2010),[3]Ganade de Araujo *et al.* (2016), [4]Barfod *et al.* (2004), [5]Amedjoe *et al.* (2018), [6]Anani (1999), [7]Anani *et al.* (2013), [8]Anani *et al.* (2017), [9]Clauer (1976), [10]Osae *et al.* (2006), [11]Kwayisi *et al.* (2022b) [12]Clauer *et al.* (1982), [13]Anani *et al.* (2019) and [14]Ganade de Araujo *et al.* (2014b). WAC = West African Craton, BNS = Benino-Nigerian Shield.

Supergroup (i.e., Kwahu-Bombouaka Group) (Table 1; Anani *et al.*, 2019; Kwayisi *et al.*, 2022b). Besides, a passive margin setting of deposition was inferred by Kalsbeek *et al.* (2008) because of U-Pb detrital zircon ages population between 2200 and 930 Ma of the quartzite in the TSU which accumulated sediments mainly from the West African–Amazonian cratons (Kalsbeek *et al.*, 2008). Also, detrital zircon grains in sediments related to the active margin of the Dahomeyide belt vary from 781 to 617 Ma (Ganade de Araujo *et al.*, 2016). Given that, Kwayisi *et al.* (2022b) correlated the TSU, Buem structural unit and the Kwahu-Bombouaka Group to have deposited in a similar depositional (passive margin) setting with the same provenance. Petrographical and geochemical data, which can better constrain the provenance and depositional setting of the quartzite of the TSU, are generally lacking. Thus, there is a need to carry out comprehensive petrographical and geochemical studies of the quartzites of the TSU to evaluate their provenance and depositional setting and compare the result to the siliciclastic rocks of the Buem structural unit and Kwahu-Bombouaka Group.

1.b. Field relations, petrography and structures

Rocks of the TSU encountered in the field are quartzites and phyllites, which form several broadly NNE-SSW to North-South-trending hills and valleys. The quartzites dominate over the phyllites in terms of volume. Two types of quartzite occur in the field: foliated and massive quartzites (Fig. 4a and 4b). The foliated quartzite shows both thick and thin foliations, with the foliation striking generally N-S in the northern section and NE-SW in the southern section with moderate to steep dips to the East or SE.

Medium to coarse-grained characterized the foliated quartzites. They are dominantly composed of quartz with a minor amount of mica and feldspar (Fig. 4c). The grains are sub-rounded to rounded, sutured, with few being slightly elongated and preferred oriented. Few are highly strained, showing mylonitic texture (Fig. 4d). The quartz grains are stained with undulose extinction. Trace amounts of relict lithic fragments, mostly metamorphic materials and micas, also occur. The massive quartzites are composed almost entirely of course-grained quartz grains with small amounts of feldspar, mica grains and lithic fragments (Fig. 4e) and sometimes show cataclastic texture (Fig. 4f). The phyllites observed are of two varieties: the dark grey and whitish phyllites (Fig. 5a). In general, the phyllites are fine-grained with a silky sheen lustre. They contain clast of quartz, mica, chlorite and carbonaceous matter (mostly in the dark grey variety) minerals (Fig. 5b). Dominant structures observed in the phyllites include crenulations, cleavages and joints. Occasionally, the phyllites and foliated quartzite are intercalated (Fig. 5a). Table 2 presents the modal composition of the quartzites. The framework grains of the studied quartzites, which are characterized by dominant quartz grains with a minor amount of feldspars and relict lithic fragments, are classified as quartz arenite and sublitharenite with one sample each plotting as subarkose and arkose (Fig. 6).

The TSU rocks are folded with the folding expressed as recumbent, isoclinal and crenulations (Fig. 7a and 7b). Foliation,

https://doi.org/10.1017/S001675682400027X

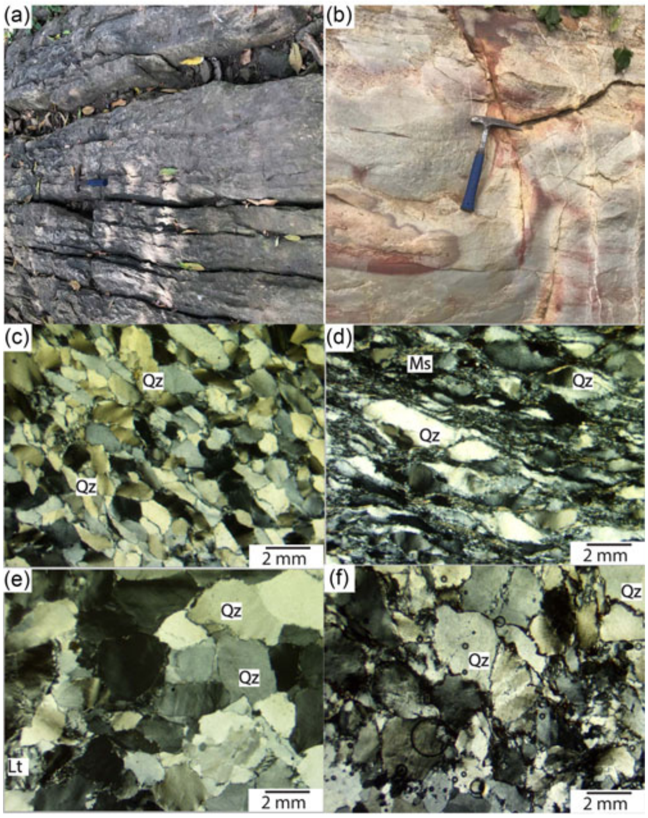

Figure 4. Field photos of (a) foliated quartzite and (b) massive quartzite, photomicrographs of (c) foliated quartzite showing elongated quartz grains in a preferred orientation, (d) foliated quartzite showing proto-mylonitic texture, (e) massive quartzite and (f) massive quartzite showing cataclastic texture. All photomicrographs were taken in crossed polars. Qz = quartz, Ms = muscovite and Lt = lithic fragment. Mineral abbreviations are from Dickinson *et al.* (1983) and Whitney and Evans (2010).

folds, lineation, faults, joints and thrust contacts define three main deformational events the TSU's rocks have undergone. D1, which is expressed by S1 tectonic foliation, is not well preserved and has a partially or wholly transposed S0 bedding plane. S1 is axial planar to F1 recumbent folds, which strikes 030-040° NE and dips between 04-05° SE (Fig. 7a). F1 have an east plunging B1 fold axis with near horizontal plunges.

The dominant deformational event is the D2, which is widespread throughout the entire TSU. D2 is characterized by S2 tectonic foliations, F2 isoclinal and crenulation folds (that are cylindrical at the mesoscale; Fig. 7b). The crenulation is observed mainly in the phyllites. S2 strikes 340–358° NNW-SSE and dips between 45° and 70° to the east, and this is akin to rocks of the Buem structural unit (Kwayisi *et al.*, 2020). F2 has a west-verging axial plane and an N-plunging B2 fold axis. Contained in the S2 foliation are downdip L2 stretching lineations (Fig. 7c). In thin-section, the S2 is expressed as the elongation and preferred orientation of quartz, mica and chlorite in the quartzite and phyllites (Fig. 7d). Late joints and faults characterized the D3 deformation (Figs. 4a, 4b, and 7c).

1.c. Analytical procedure

A total of 51 rock samples were analysed for their major and trace element compositions at the ALS laboratory in Vancouver, Canada. The samples included 42 quartzites and 9 phyllites. The major elements were analysed using Inductively Coupled Plasma-Atomic Emission Spectrometry (ICP-AES), while the trace elements were analysed using multi-element fusion Inductively Coupled Plasma Mass-Spectrometry (ICP-MS). The analytical procedure for the major and trace elements analyses is described in Nude *et al.* (2015) and Kwayisi *et al.* (2017). Fusing in a furnace of approximately 0.200 g of the prepared sample with lithium at 1025°C was done for the purpose of major element analysis. The resulting melt was then dissolved in an acidic solution consisting of Nitric (NH_3) + hydrochloric (HCl) and hydrofluoric (HF) acids after being cooled. The solution was analysed for the concentrations of major elements using ICP-AES. With a temperature of 1000°C, loss on ignition was determined. Similar procedures were used for the trace element analysis. However, in this instance, 0.100 g of the prepared sample was weighed, and ICP-MS was used for the analyses. ICP-AES was used to analyse the base metals after the 0.25 g prepared sample was digested with perchloric, NH_3, HCl and HF acids. The residue was then treated with diluted HCl, and the ICP-AES was used to analyse the solution. The results were corrected for spectral inter-element interferences (ALS laboratory). Precision and accuracy are better than 3% for the major elements and 10% for the trace elements.

2. Results

2.a. Major elements

The studied quartzites have SiO_2 content in the range of 82.07 – 99.0 wt % (Table 3). These SiO_2 values are higher than those of the phyllites, which have values between 70.50 and 89.20 wt %. Al_2O_3 is higher in the phyllites (Al_2O_3 = 6.68 – 16.37 wt %, avg. 12.23 wt %) and lower in the quartzites (Al_2O_3 = 0.22 – 7.98, avg. 1.91 wt %). The ferromagnesian elements are relatively higher in the phyllites (Fe_2O_3t = 1.24 – 5.94, avg. 2.59 wt % and MgO = 0.37 – 1.81, avg. 0.74 wt %) than the quartzites (Fe_2O_3t = 0.31 – 2.90, avg. 0.96 wt % and MgO = 0.01 – 0.32, avg. 0.09 wt %). K_2O content varies with the higher content observed in the phyllites (2.14 – 5.22, avg. 3.46 wt %). K_2O contents of the quartzites are low in the range of 0.04 – 3.24, avg. 0.47 wt %. Major elements ratios of Al_2O_3/TiO_2 are nearly similar for all the studied rocks of the TSU and akin to Upper Continental Crust (UCC) but slightly higher than Post Archean Australian Shale (PAAS) (Table 3).

2.b. Trace elements

The trace element concentrations of the quartzites and phyllites of the TSU are presented in Table 3. The studied rocks of the TSU exhibit a similar REE pattern comparable to UCC and PAAS on the REE-diagrams normalized to chondrite (Fig. 8), characterized by Light Rare Earth Elements (LREE) enrichment relative to Heavy Rare Earth Element (HREE) and also negative EU anomaly. The quartzites in general, have lower overall REE concentrations than the phyllites (Fig. 8). Figure 9 shows the UCC-normalized multi-element diagrams for the studied quartzites and phyllites of the TSU. On these diagrams, the studied rocks display strong Sr depletion akin to PAAS. In general, the patterns depicted by the studied rocks appear to resemble that of PAAS, however, with significant variations (Fig. 9). The studied quartzites and phyllites display negative Ba, P, Nb-Ta and Ti peaks compared to PAAS.

https://doi.org/10.1017/S001675682400027X

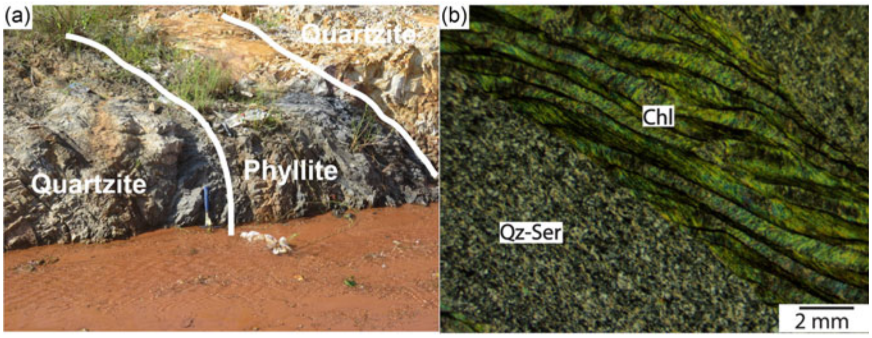

Figure 5. (a) Field photo of phyllite interbedded in foliated quartzite and (b) photomicrographs of phyllite showing quartz–seritcite–chlorite mineral assemblage. The photomicrographs were taken in cross-polars. Qz = quartz, Pl = plagioclase, Chl = chlorite and Lt = lithic fragment. Mineral abbreviations are from Dickinson *et al.* (1983) and Whitney and Evans (2010).

3. Discussion

3.a. Influence of metamorphism on elemental mobility

The presence of chlorite, sericite and quartz observed from the petrographic investigation in this study points to greenschist-facies metamorphism. It is thus crucial to assess how metamorphism affects the mobile elements in the TSU. High Field Strength Element (HFSE) and REEs are generally not affected when siliciclastic rocks are metamorphosed. The rocks in the TSU exhibit an REE pattern similar to PAAS (Fig. 9), which is unexpected if the elements were remobilized during metamorphism (McLennan & Taylor, 1991; Girty *et al.*, 1994). Therefore, the trace elements display chemical uniformity and data homogeneousness, implying that there was no significant remobilization at a large scale.

3.b. Maturity and recycling of the sediments

The modal composition of the quartzites varies from 88 to 99% quartz that is rounded to sub-rounded (Fig. 4c and 4e). These imply that the quartzites are texturally and mineralogical mature with high recycling due to either long-distance travel or long periods at the depositional basin. However, they have been metamorphosed and deformed during the Pan-African orogeny, evident in the sutured grain contacts and elongation (Fig. 4). Maturity in siliciclastic rocks can be tested using the SiO_2/Al_2O_3 and Na_2O/K_2O ratios (Dabard, 1990; Armstrong-Altrin, 2015). High SiO_2/Al_2O_3 (> 10) and low Na_2O/K_2O (<1) ratios are characteristics of mature siliciclastic rocks (Dabard, 1990; Armstrong-Altrin, 2009, 2015). The quartzites have high values of SiO_2/Al_2O_3 (>10; Table 3) and low Na_2O/K_2O (<1) values, and these, coupled with their high quartz content, suggest they are composed of mature sediments. The phyllites, on the other hand, have low SiO_2/Al_2O_3 (<10) and low Na_2O/K_2O (<0.1, respectively), which, except for two samples with high SiO_2/Al_2O_3, suggest immature sediment. Recycling of sediments within the sedimentary basin can be inferred from the Zr/Sc ratio because, during sorting and recycling, the ratio of Zr/Sc increases due to the addition of zircon (McLennan *et al.*, 1993). Usually, variation in the geochemical composition of siliciclastic rocks due to variation in the source rock (i.e., mafic and felsic rocks) may result in a strong positive correlation on the Th/Sc versus Zr/Sc diagram, whereas sedimentary recycling will result in higher ratios than UCC and PAAS. The studied rocks of the TSU have a wide range of Zr/Sc and Th/Sc ratios (Fig. 10), which are higher than UCC and PAAS, indicating a significant recycling process, and thus, the rocks are composed of mature sediments. Compared to the shales, siltstones, sandstones and phyllites of the Buem and TSUs and Kwahu-Bombuaka Group, the studied rocks show similar Zr/Sc and Th/Sc ratios. This may suggest similar sediment maturity and recycling.

3.c. Provenance

Medium to coarse sand-size quartz is the dominant grain in the quartzites, which may suggest sediment from a felsic proto-source such as granitoid, gneiss or pre-existing quartz-rich sandstone. The phyllites, conversely, contain micas and chlorite, which suggest pelitic proto-source rocks such as shale with significant mafic input. Generally, the ratio of LREE/HREE is high in felsic igneous rocks and low in mafic igneous rocks (Cullers, 1994). Mafic and felsic igneous rocks usually have Eu anomaly of 0.8 – 1 and 0.5 – 0.8, respectively (McLennan *et al.*, 1993). Accordingly, the ratio of LREE/HREE and the Eu anomaly have been used to infer the proto-source rock of sedimentary rocks (e.g., McLennan, 1989). The rocks of the TSU all show a higher LREE/HREE ratio (5.72 – 13.32; Table 3) and significant negative Eu anomalies (0.6 – 0.8; 3; Fig. 9). In view of that, the provenance of the rocks of the TSU can be explained as sedimentary deposits dominated by detritus derived from intermediate and felsic proto-source rocks. Ratios of La/Sc, Th/Sc, Eu/Eu* and $(La/Lu)_N$ provide information about the composition of the source rock (Cullers *et al.*, 1988; Cullers, 1994, 2000). The elemental ratios of the rocks of the TSU suggest their sediments were derived from a felsic source rock (Table 4). Since some of the ratios overlap between felsic and mafic rocks, especially for the phyllites, it would suggest a significant contribution from a mafic rock. These elemental ratios are akin to siliciclastic rocks of the Buem structural unit and the Kwahu-Bombuaka Group of the Voltaian Supergroup, which might suggest similar source rocks. Overall, both felsic and intermediate proto sources contributed significant sediments to the rocks of the TSU. Available U-Pb detrital zircon age population of the quartzites from the TSU range between 2200 and 930 Ma, with abundant Mesoproterozoic (1600 – 1000 Ma) zircon grains, which are yet to be found on the West African Craton but abundant on the Amazonian Craton (Kaslbeek *et al.*, 2008; Ganade de Araujo *et al.*, 2016). Therefore, the most likely sources for this sediment are the basement granitoid, granitic gneisses and/or sedimentary rocks of the West African Craton and/or Amazonian Craton.

3.d. Depositional setting of the rocks of the TSU

The mineralogical and geochemical compositions of siliciclastic rocks offer important information regarding the depositional setting of the source rocks (Armstrong-Alrin *et al.*, 2015). The main assumption is that different tectonic settings impact different mineralogical compositions and unique geochemical features on siliciclastic rocks that are usually retained in the sediments via diverse sedimentary processes (Dickinson *et al.*, 1983; Armstrong-Alrin *et al.*, 2015; Verma & Armstrong-Altrin, 2016). Consequently, Anani *et al.* (2019), on the basis of mineralogical

https://doi.org/10.1017/S001675682400027X

Table 2. Mineralogical compositions of the quartzites of the TSU

	Qm	Qp	K	P	Ls	Lm	M	Q	F	L	Qm	F	Lt
DK1	92.3	5.15	0	2.04	0	0.51		97.45	2.04	0.51	92.3	2.04	5.66
DK2	94.05	5.55	0	0.32	0	0.08		99.6	0.32	0.08	94.05	0.32	5.63
DK3	93.6	5.05	0	1.08	0	0.27		98.65	1.08	0.27	93.6	1.08	5.32
DK4	91.45	5.7	0	2.28	0	0.57		97.15	2.28	0.57	91.45	2.28	6.27
DK8	98.6	0.4	0	0	0	0		99	1	0	98.6	1	0.4
DK9	96	2.6	0	1.4	0	1.4		98.6	1.4	0	96	1.4	2.6
DK10	100	0	0	0	0	0		100	0	0	100	0	0
DK11	99	0.8	0	0	0	0		99.8	0.2	0	99	0.2	0.8
DK12	99.6	0	0.4	0	0	0.4		99.6	0.4	0	99.6	0.4	0
DK13	85.6	1.8	0	0	0	0		87.4	3.4	9.2	85.6	3.4	11
DK14	97.6	2	0	0	0	0		99.6	0	0.4	97.6	0	2.4
DK15	92.8	5.6	0.6	0.8	0	1.4		98.4	1.4	0.2	92.8	1.4	5.8
DK16	99.8	0	0	0.2	0	0.2		99.8	0.2	0	99.8	0.2	0
DK29	98.4	1.6	0	0	0	0		100	0	0	98.4	0	1.6
DK30	98.4	1.4	0	0.2	0	0.2		99.8	0.2	0	98.4	0.2	1.4
DK31	99.4	0	0	0.6	0	0.6		99.4	0.6	0	99.4	0.6	0
DK32	98.6	1.4	0	0	0	0		100	0	0	98.6	0	1.4
DK35	96.6	3.4	0	0	0	0		100	0	0	96.6	0	3.4
DK36	99	0	0	0	0	0		99	1	0	99	1	0
DK39	89.8	0	0	0	0	0		89.8	3.2	7	89.8	3.2	7
DK40	99	0	0	0	0	0		99	1	0	99	1	0
DK41	72.4	0.4	0	26.6	0	26.6		72.8	26.6	0.6	72.4	26.6	1
DK42	84.8	1.2	12.6	1.4	0	14		86	14	0	84.8	14	1.2
DK46	90.3	6.3	0	2.3	0	1		96.6	2.3	1.1	90.3	2.3	7.4
DK47	83	5.3	0.7	9.7	0	0.7		88.3	10.4	1.3	83	10.4	6.6
DK48	90.7	5.3	0	1.3	0	2.7		96	1.3	2.7	90.7	1.3	8
DK49	93	3.7	0	1	0	2.3		96.7	1	2.3	93	1	6
DK50	96	3	0	0.7	0	0.3		99	0.7	0.3	96	0.7	3.3
DK53	96	3	0	0	0	1		99	0	1	96	0	4
DK54	100	0	0	0	0	0		100	0	0	100	0	0
DK55	93	3.7	0	1	0	2.3		96.7	1	2.3	93	1	6
DK57	96	3	0	0.7	0	0.3		99	0.7	0.3	96	0.7	3.3
DK61	96	3	0	0	0	1		99	0	1	96	0	4
DK62	90.3	6.3	0	2.3	0	1		96.6	2.3	1.1	90.3	2.3	7.4
DK68	83	5.3	0.7	9.7	0	0.7		88.3	10.4	1.3	83	10.4	6.6
DK70	90.7	5.3	0	1.3	0	2.7		96	1.3	2.7	90.7	1.3	8
DK71	97	1	0	0	1.4	0.6		98	0	2	97	0	3
DK5	91.6	7.35	0	0.84	0	0.21		98.95	0.84	0.21	91.6	0.84	7.56
DK52	91.1	7.5	0	1.12	0	0.28		98.6	1.12	0.28	91.1	1.12	7.78
DK26	94.45	4.8	0	0.6	0	0.15		99.25	0.6	0.15	94.45	0.6	4.95
DK26	91.5	7.1	0	1.12	0	0.28		98.6	1.12	0.28	91.5	1.12	7.38
DK51	91.6	7.2	0	0.96	0	0.24		98.8	0.96	0.24	91.6	0.96	7.44
DK27	91.1	7.65	0	1	0	0.25		98.75	1	0.25	91.1	1	7.9

(*Continued*)

https://doi.org/10.1017/S001675682400027X

Table 2. (*Continued*)

	Qm	Qp	K	P	Ls	Lm	M	Q	F	L	Qm	F	Lt
DK28	91.55	8.05	0	0.32	0	0.08		99.6	0.32	0.08	91.55	0.32	8.13
DK58	91.6	7.3	0	0.88	0	0.22		98.9	0.88	0.22	91.6	0.88	7.52
DK59	97.85	0.9	0	1	0	0.25		98.75	1	0.25	97.85	1	1.15
DK60	93.4	1.05	0	4.44	0	1.11		94.45	4.44	1.11	93.4	4.44	2.16
DK66	91.45	7.3	0	1	0	0.25		98.75	1	0.25	91.45	1	7.55
DK67	91.925	6.5	0	1.26	0	0.315		98.425	1.26	0.315	91.925	1.26	6.815
DK17	92.8	2	2	0.2	2.4	0.6		94.8	2.2	3	92.8	2.2	5
DK18	100	0	0	0	0	0		100	0	0	100	0	0
DK19	76.1	4.2	10.5	2.8	5	1.4		80.4	13.3	6.3	76.1	13.3	10.6
DK20	80.6	6.9	7.9	2	2.4	0.3		87.5	9.8	2.7	80.6	9.8	9.6
DK21	81.6	5.9	8.1	1.7	1.4	1.4		87.5	9.7	2.8	81.6	9.7	8.7
DK22	81.3	6.9	8.2	2.3	0.8	0.5		88.2	10.5	1.3	81.3	10.5	8.2
DK23	90.3	6.3	0	2.3	0	1.1		96.6	2.3	1.1	90.3	2.3	7.4
DK24	83.6	5.3	0.7	9.7	0	0.7		88.9	10.4	0.7	83.6	10.4	6
DK25	90.7	5.3	0	1.3	0	2.7		96	1.3	2.7	90.7	1.3	8
DK1	92.3	5.15	0	2.04	0	0.51		97.45	2.04	0.51	92.3	2.04	5.66
DK2	94.05	5.55	0	0.32	0	0.08		99.6	0.32	0.08	94.05	0.32	5.63
DK3	93.6	5.05	0	1.08	0	0.27		98.65	1.08	0.27	93.6	1.08	5.32
DK4	91.45	5.7	0	2.28	0	0.57		97.15	2.28	0.57	91.45	2.28	6.27

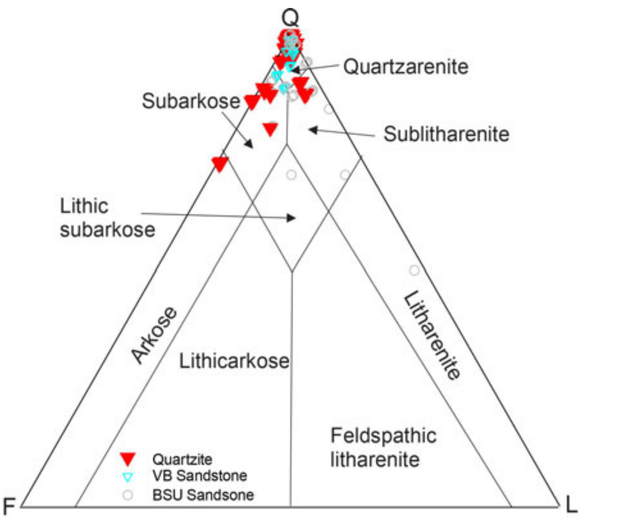

Figure 6. QFL diagram (Dickinson *et al.*, 1983) for the quartzites of the TSU compared with the sandstones of the Buem structural unit (Osae *et al.*, 2006; Kwayisi *et al.*, 2022b) and the Kwahu-Bombouaka Group of the Voltaian Supergroup (Anani *et al.*, 2017). Q = quartz, F = feldspar and L = lithic fragment (excluding polycrystalline quartz).

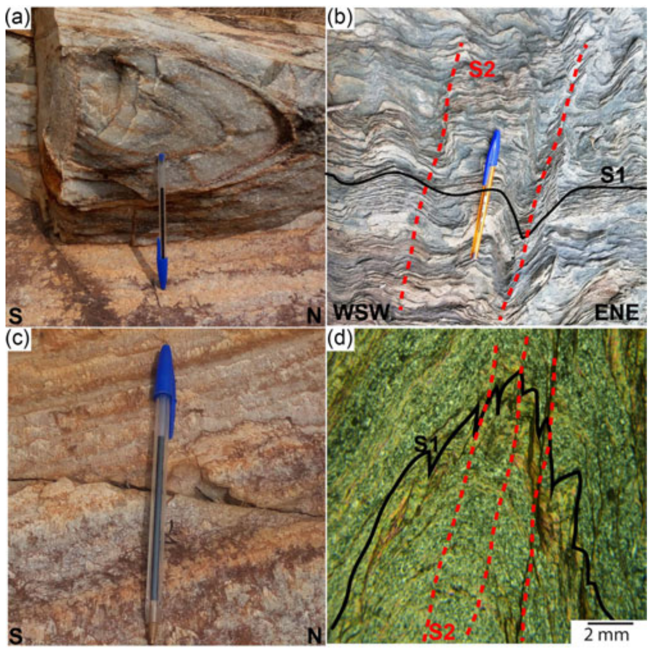

Figure 7. (a) F1 recumbent fold with near horizontal axial plane, (b) partially transposed S1 foliation by D2 event and the development of S2 foliation, (c) down-dip stretching L2 lineation on S2 foliation plane and (d) photomicrograph showing the relationship between S1 and S2 foliation plane in microscopic view (crossed polars).

and geochemical studies of the phyllites of the TSU, proposed a passive margin depositional setting (Table 1). Nevertheless, because of a U-Pb zircon age population of 2200 – 930 Ma, Kalsbeek *et al.* (2008) inferred a passive margin setting for the quartzites of the TSU. This is attributed to the passive margin sequence in the Dahomeyide belt and the West Gondwana orogen having the youngest detrital U-Pb ages >900 Ma (Kalsbeek *et al.*, 2008; Ganade de Araujo *et al.*, 2016; Caxito *et al.*, 2020; Kwayisi *et al.*, 2022b). In this study, the framework grains are used together with the geochemistry to determine the depositional setting of the

https://doi.org/10.1017/S001675682400027X

Table 3. Whole-rock major and trace elements compositions of the rocks of the TSU

	DK6	DK7	DK34	DK43	DK56	DK63	DK64	DK65	DK69
wt %					Phyllite				
SiO_2	70.5	71.3	78.2	74.6	73.6	89.2	85.6	82	72.2
TiO_2	0.75	0.73	0.58	0.71	0.73	0.2	0.33	0.51	0.7
Al_2O_3	16.37	11.72	11	14.45	15.3	6.68	8.54	10.35	15.7
Fe_2O_3	2.93	5.94	3.77	2.19	1.69	1.24	1.34	1.29	2.97
MnO	0.01	0.02	0.02	0.01	0.01	0.01	0.01	0.01	0.01
MgO	0.58	1.81	0.79	0.81	0.78	0.37	0.47	0.58	0.46
CaO	0.06	0.18	0.01	0.01	0.01	0.01	0.01	0.01	0.01
Na_2O	0.13	1.59	0.03	0.06	0.06	0.04	0.04	0.03	0.16
K_2O	4.03	2.52	3.2	4.47	5.22	2.14	2.74	3.37	3.53
P_2O_5	0.026	0.106	0.02	0.03	0.02	0.02	0.01	0.03	0.03
LOI	3.79	3.66	2.97	3.01	2.47	1.27	1.63	1.76	4.71
Total	99.25	99.73	100.64	100.45	99.98	101.17	100.71	99.93	100.56
Na_2O/K_2O	0.0	0.6	0.0	0.0	0.0	0.0	0.0	0.0	0.0
SiO_2/Al_2O_3	4.3	6.1	7.1	5.2	4.8	13.4	10.0	7.9	4.6
Al_2O_3/TiO_2	22	16	19	20	21	33	26	20	22
CIA	71	65	68	67	65	66	66	66	73
CIW	98	83	99	99	99	99	99	99	99
ppm									
Rb	135.5	76.7	111	143.5	162	64.2	79.7	97.6	145
Ba	699	1215	433	950	719	361	468	560	648
Th	15.2	8.02	7.53	14.45	13.05	4.17	6.52	9.76	16.25
U	4.17	1.73	2.14	3.26	3.64	1.13	1.71	2.42	4.64
K	33449	20916	26560	37101	43326	17762	22742	27971	29299
Nb	14.8	11	9.1	14.7	14.3	4.5	6.7	9.8	16.2
Ta	1	0.7	0.7	1	1	0.3	0.5	0.7	0.1
La	37.5	31.7	21.8	46.5	42	21.9	32.4	26.2	38.2
Ce	75.4	50.3	41.7	107.5	92.7	50.9	73.2	55.6	73.6
Sr	28.3	46	15.2	25.5	29.1	9.4	10.8	10.6	52.1
Nd	33.4	28.8	17.8	48	42.8	18.7	27.6	21.5	33.9
P	113.36	462.16	87.2	130.8	87.2	87.2	43.6	130.8	130.8
Hf	11.2	5.9	7	12	15.8	8.3	9.5	15.3	12.9
Zr	434	223	238	407	331	306	380	625	499
Sm	6.35	5.84	3.69	9.05	10.05	3.41	4.94	3.9	7.41
Ti	4492.5	4372.7	3474.2	4252.9	4372.7	1198	1976.7	3054.9	4193
Tb	0.84	0.91	0.62	1.13	0.87	0.37	0.47	0.54	1.31
Y	30.3	31.2	22.9	34.4	30.7	12.7	16.7	20.7	44.6
Tm	0.56	0.42	0.4	0.52	0.51	0.2	0.28	0.33	0.65
Yb	3.78	2.39	2.52	3.01	3.72	1.46	1.98	2.6	4.54
Sc	1.5	2	3	3	2.5	2	2	3.5	3
Cs	2.25	4.95	4.12	3.86	1.88	1.13	1.61	2	5.21
Dy	5.37	5.2	3.86	6.29	5.71	2.32	3.2	3.49	0.78
Er	3.57	3.02	2.58	3.5	3.4	1.31	2.06	2.44	0.29

(*Continued*)

https://doi.org/10.1017/S001675682400027X

Table 3. (*Continued*)

	DK6	DK7	DK34	DK43	DK56	DK63	DK64	DK65	DK69
Eu	0.99	1.22	0.63	1.87	1.38	0.55	0.74	0.65	1.83
Ga	20.5	15.6	12.3	18.5	21.1	7.4	10.1	12.5	
Gd	5.43	6.28	3.45	7.29	6.5	2.52	3.48	3.71	7.56
Ho	1.17	1.06	0.84	1.31	1.03	0.49	0.57	0.72	0.06
Cr	60	60	170	40	60	40	40	40	50
Lu	0.53	0.39	0.38	0.57	0.53	0.22	0.26	0.37	0.69
Pr	8.68	7.59	4.99	12.5	11.2	5.75	7.78	6.22	0.73
V	81	87	47	70	74	19	32	42	80

	DK8	DK9	DK10	DK11	DK12	DK13	DK14	DK15	DK16	DK29	DK30	DK31
wt %						Quartzite						
SiO_2	95.72	94.13	96.66	98.56	97.33	97.4	97.54	97.5	97.62	99.2	99.1	99.1
TiO_2	0.04	0.05	0.03	0.03	0.02	0.02	0.03	0.03	0.06	0.02	0.05	0.03
Al_2O_3	1.16	1.59	1.25	0.44	0.31	0.39	0.73	0.53	1.04	0.4	1.2	0.47
Fe_2O_3	1.2	2.9	1.1	1.14	0.94	0.9	0.98	0.86	0.81	0.44	0.52	0.41
MnO	0.01	0.18	0.01	0.01	0.01	0.01	0.01	0.01	0.01	0.02	0.01	0.01
MgO	0.11	0.16	0.07	0.04	0.03	0.04	0.2	0.04	0.05	0.01	0.08	0.01
CaO	0.05	0.02	0.01	0.04	0.02	0.03	0.01	0.02	0.02	0.02	0.02	0.01
Na_2O	0.08	0.05	0.03	0.04	0.03	0.04	0.02	0.03	0.02	0.03	0.02	0.01
K_2O	0.27	0.33	0.38	0.1	0.09	0.12	0.25	0.16	0.24	0.1	0.28	0.12
P_2O_5	0.012	0.011	0.008	0.025	0.006	0.006	0.006	0.007	0.006	0.02	0.02	0.01
LOI	0.27	0.63	0.17	2	0.01	0.05	0.03	0.08	0.24	0.03	0.37	0
Total	98.94	100.05	99.74	100.4	98.78	99.01	99.8	99.26	100.1	100.31	101.7	100.23
Na_2O/K_2O	0.3	0.2	0.1	0.4	0.3	0.3	0.1	0.2	0.1	0.3	0.1	0.1
SiO_2/Al_2O_3	82.5	59.2	77.3	224.0	314.0	249.7	133.6	184.0	93.9	248.0	82.6	210.9
Al_2O_3/TiO_2	29	32	42	15	16	20	24	18	17	20	24	16
CIA	66	72	66	62	60	58	63	62	71	64	71	69
CIW	87	94	96	80	82	80	95	88	95	85	96	94
ppm												
Rb	8.5	11.3	11.3	2.5	2.3	3.7	5.2	4.4	6.7	2.5	10.2	3.4
Ba	51.9	183	62	17.8	15.2	33.7	27.9	19.6	43.4	38.8	49.2	91.9
Th	1.11	0.99	1.24	0.71	0.91	0.72	1.09	0.76	1.18	0.53	1.45	1.04
U	0.32	0.55	0.27	0.24	0.43	0.23	0.32	0.21	0.41	0.21	0.43	0.27
K	2241	2739	3154	830	747	996	2075	1328	1992	830	2324	996
Nb	0.9	1.3	0.9	0.8	0.7	0.7	1	0.7	1.5	0.5	1.1	0.6
Ta	0.1	0.1	0.1	0.1	0.1	0.1	0.1	0.1	0.1	0.1	0.1	0.1
La	14.4	6.4	9.7	2.8	3.8	0.4	5.8	3.4	4.5	1.9	17.2	4.1
Ce	19.5	19	15.1	5.3	5.6	6.6	23.6	7.9	7.7	5.9	39	7.3
Sr	10.3	10.8	7.7	7	5.6	5.7	1.6	5.3	5.8	14.3	8.6	6
Nd	8	9.5	6.7	2.1	2.2	2.8	9	3.2	3.2	2.4	17.6	3
P	52.32	47.96	34.88	109	26.16	26.16	26.16	30.52	26.16	87.2	87.2	43.6
Hf	1.2	1.4	0.8	0.9	1	0.5	1	0.8	1.6	0.6	1.3	1
Zr	48	53	28	33	36	22	40	33	65	22	47	36
Sm	1.29	1.86	1.3	0.46	0.46	0.46	1.55	0.53	0.55	0.42	3.69	0.54

(*Continued*)

https://doi.org/10.1017/S001675682400027X

Table 3. (*Continued*)

	DK8	DK9	DK10	DK11	DK12	DK13	DK14	DK15	DK16	DK29	DK30	DK31
Ti	239.6	299.5	179.7	179.7	119.8	119.8	179.7	179.7	359.4	119.8	299.5	179.7
Tb	0.13	0.25	0.13	0.06	0.06	0.03	0.15	0.05	0.09	0.06	0.29	0.06
Y	2.8	7.5	3	1.9	2.1	1.5	3.7	1.6	2.6	1.8	6.1	2.3
Tm	0.03	0.11	0.05	0.03	0.03	0.02	0.05	0.02	0.05	0.03	0.07	0.04
Yb	0.24	0.56	0.29	0.22	0.28	0.17	0.34	0.16	0.29	0.19	0.43	0.24
Sc	1	0.5	1.75	2	2.25	2.25	3	2.25	1.25	1	2.5	1.75
Cs	0.1	0.24	0.1	0.02	0.02	0.05	0.02	0.05	0.07	0.05	0.15	0.04
Dy	0.59	1.3	0.59	0.3	0.33	0.31	0.78	0.27	0.44	0.32	1.51	0.37
Er	0.31	0.65	0.29	0.21	0.24	0.16	0.48	0.14	0.34	0.18	0.55	0.24
Eu	0.19	0.35	0.16	0.09	0.06	0.07	0.26	0.09	0.08	0.08	0.49	0.08
Ga	1.8	2.8	1.7	1	1	1	1.1	1.1	1.4	0.6	1.4	0.7
Gd	0.85	1.67	0.89	0.34	0.41	0.4	1.11	0.35	0.52	0.35	2.17	0.43
Ho	0.1	0.25	0.09	0.08	0.08	0.06	0.17	0.06	0.08	0.05	0.24	0.07
Cr	20	20	20	20	30	30	20	10	20	390	320	380
Lu	0.05	0.11	0.05	0.03	0.04	0.03	0.05	0.02	0.05	0.02	0.06	0.03
Pr	2.11	2.36	1.78	0.58	0.58	0.73	2.39	0.85	0.89	0.67	4.77	0.86
V	7	11	5	5	5	5	5	5	5	5	5	5
	DK32	DK35	DK36	DK39	DK40	DK41	DK42	DK46	DK47	DK48	DK49	DK50
wt %						Quartzite						
SiO_2	94.2	92.5	96.4	99.7	97.9	95.6	96.9	99.6	97.33	84.7	98.56	82.07
TiO_2	0.05	0.13	0.05	0.04	0.02	0.05	0.02	0.03	0.02	2.37	0.03	0.42
Al_2O_3	2.78	3.36	1.89	0.46	0.71	2.08	0.29	1.25	0.31	5.77	0.44	7.98
Fe_2O_3	1.27	1.56	0.61	0.42	0.63	0.46	0.57	1.1	0.94	2.36	1.14	2.65
MnO	0.02	0.01	0.01	0.01	0.01	0.01	0.01	0.01	0.01	0.02	0.01	0.02
MgO	0.23	0.21	0.16	0.06	0.03	0.16	0.01	0.07	0	0.4	0.04	0.16
CaO	0.01	0.01	0.01	0.08	0.01	0.01	0.02	0.01	0.02	0.07	0.04	0.07
Na_2O	0.02	0.01	0.01	0.04	0.03	0.02	0.01	0.03	0.03	0.06	0.04	0.08
K_2O	1.26	1.35	0.66	0.11	0.23	0.72	0.06	0.38	0.09	1.94	0.1	3.24
P_2O_5	0.01	0.01	0.01	0.01	0.01	0.01	0.01	0.008	0.006	0.072	0.025	0.068
LOI	0.41	0.58	0.3	0.11	0.14	0.41	0.1	0.17	0.01	1.26	0.02	1.34
Total	100.35	99.79	100.17	101.04	99.72	99.53	98	99.74	98.78	99.11	100.4	98.15
Na_2O/K_2O	0.0	0.0	0.0	0.4	0.1	0.0	0.2	0.1	0.3	0.0	0.4	0.0
SiO_2/Al_2O_3	33.9	27.5	51.0	216.7	137.9	46.0	334.1	79.7	314.0	14.7	224.0	10.3
Al_2O_3/TiO_2	56	26	38	12	36	42	15	42	16	2	15	19
CIA	58	61	64	58	63	64	68	66	60	64	62	60
CIW	99	99	99	74	93	98	88	96	82	97	80	97
ppm												
Rb	40.1	42	21.9	3.3	7.2	21.5	1.7	11.3	2.3	58	2.5	88
Ba	292	297	141.5	40.7	56.7	152.5	15.3	62	15.2	319	17.8	391
Th	1.81	2.94	1.78	1.31	0.88	1.11	0.55	1.24	0.91	42.3	0.71	13.45
U	0.57	0.71	0.39	0.35	0.27	0.57	0.21	0.27	0.43	6.97	0.24	2.28
K	10458	11205	5478	913	1909	5976	498	3154	747	16102	830	26892
Nb	1.1	2.7	1	1.5	1.1	1.4	0.4	0.9	0.7	43	0.8	8.4

(*Continued*)

https://doi.org/10.1017/S001675682400027X

Table 3. (*Continued*)

	DK32	DK35	DK36	DK39	DK40	DK41	DK42	DK46	DK47	DK48	DK49	DK50
Ta	0.1	0.2	0.1	0.1	0.1	0.1	0.1	0.1	0.1	3.6	0.1	0.6
La	9.6	9.4	7.9	11.8	1.3	9.9	0.8	8.2	2.3	75.2	3.4	23.5
Ce	36.8	18.8	23.3	24.9	7.5	22.6	4.4	15.1	5.6	158	5.3	71
Sr	15.7	10.1	10.9	6.1	6.1	4.7	4	7.7	5.6	36.4	7	42.8
Nd	17	7.9	10.6	9.9	2.9	10.7	1.7	6.7	2.2	63.1	2.1	33.8
P	43.6	43.6	43.6	43.6	43.6	43.6	43.6	34.88	26.16	313.92	109	296.48
Hf	2.4	4.5	1.4	0.9	0.8	2.6	0.7	0.8	1	58.9	0.9	9.5
Zr	89	161	50	94	76	77	114	144	97	114	75	112
Sm	3.23	1.66	1.79	2.05	0.59	2.14	0.32	1.3	0.46	12.55	0.46	6.45
Ti	299.5	778.7	299.5	239.6	119.8	299.5	119.8	179.7	119.8	14196.3	179.7	2515.8
Tb	0.35	0.21	0.19	0.15	0.06	0.26	0.04	0.13	0.06	1.88	0.06	0.81
Y	9	6.9	5	3.5	2.1	7.4	1.2	3	2.1	61.7	1.9	27.4
Tm	0.13	0.11	0.08	0.05	0.03	0.1	0.03	0.05	0.03	1.18	0.03	0.44
Yb	0.77	0.88	0.48	0.31	0.35	0.48	0.22	0.26	0.28	8.28	0.22	3.01
Sc	1.5	1.25	1.25	1	1	1	1	1.5	1.5	1.5	2	1.5
Cs	0.6	1.11	0.54	0.16	0.2	0.4	0.06	0.1	0.02	0.64	0.02	1.06
Dy	1.77	1.17	0.98	7	0.41	1.55	0.26	0.59	0.33	11.05	0.3	4.79
Er	0.87	0.72	0.57	0.3	0.21	0.76	0.14	0.29	0.24	7.63	0.21	3.12
Eu	0.58	0.27	0.3	0.31	0.06	0.42	0.04	0.16	0.06	1.91	0.09	1
Ga	3	3.8	1.9	1	1	2.2	0.6	1.7	1	7.1	1	9.6
Gd	2.55	1.2	1.11	1.25	0.36	1.65	0.25	0.89	0.41	11.05	0.34	5.26
Ho	0.31	0.25	0.19	0.12	0.07	0.29	0.05	0.09	0.08	2.22	0.08	0.97
Cr	490	330	350	10	10	10	20	20	30	50	20	30
Lu	0.11	0.12	0.07	4	0.03	0.08	0.02	0.05	0.04	1.31	0.03	0.47
Pr	4.68	2.23	3.03	2.58	0.82	2.71	0.45	1.78	0.58	16.6	0.58	8.7
V	5	8	5	6	5	5	5	5	5	35	5	24

	DK53	DK54	DK55	DK57	DK61	DK62	DK68	DK70	DK71
wt %					Quartzite				
SiO_2	98.9	98.9	98.9	90.6	98.5	99.9	96.6	98.3	98.1
TiO_2	0.02	0.03	0.02	0.13	0.03	0.03	0.05	0.03	0.07
Al_2O_3	0.35	0.46	0.22	4.51	0.88	0.56	1.16	0.43	1.52
Fe_2O_3	0.72	0.58	0.88	1.13	0.72	0.65	0.31	0.39	0.5
MnO	0.01	0.01	0.01	0.01	0.01	0.01	0.01	0.01	0.01
MgO	0.01	0.01	0.01	0.32	0.04	0.01	0.03	0.01	0.04
CaO	0.01	0.01	0.01	0.01	0.01	0.01	0.01	0.01	0.01
Na_2O	0.02	0.02	0.03	0.04	0.01	0.02	0.01	0.01	0.01
K_2O	0.08	0.11	0.04	1.62	0.28	0.14	0.27	0.11	0.34
P_2O_5	0.01	0.02	0.02	0.03	0.01	0.01	0.01	0.01	0.02
LOI	−0.02	−0.16	−0.09	0.73	0.06	0.06	0.04	0.23	0.48
Total	100.1	98.29	99.34	99.15	100.54	101.39	99.84	99.51	101.09
Na_2O/K_2O	0.3	0.2	0.8	0.0	0.0	0.1	0.0	0.1	0.0
SiO_2/Al_2O_3	282.6	215.0	449.5	20.1	111.9	178.4	83.3	228.6	64.5
Al_2O_3/TiO_2	18	15	11	35	29	19	23	14	22

(*Continued*)

https://doi.org/10.1017/S001675682400027X

Table 3. (*Continued*)

	DK53	DK54	DK55	DK57	DK61	DK62	DK68	DK70	DK71
CIA	68	68	65	63	65	68	72	68	73
CIW	89	92	80	98	97	93	98	94	98
ppm									
Rb	2.6	3.1	1.7	51.4	9.4	4.3	10.1	4	12.8
Ba	19	98.3	32	307	55	25.5	36.6	22	55.2
Th	0.61	0.97	0.66	3.31	1.29	0.85	1.1	0.87	1.62
U	0.17	0.27	0.24	0.99	0.33	0.31	0.53	0.32	0.66
K	664	913	332	13446	2324	1162	2241	913	2822
Nb	0.3	0.8	0.2	2.8	0.5	0.5	1.3	0.7	1.4
Ta	0.1	0.1	0.1	0.2	0.1	0.1	0.1	0.2	0.1
La	2.6	7.9	1.6	25.9	7.7	3.9	6.3	2.8	8.4
Ce	5.3	14.4	4.3	47.7	14.1	5.7	9.6	5.9	29
Sr	4.8	3.8	4.7	5.5	4.1	5.1	7.4	4.9	11.6
Nd	2.1	4.7	1.4	19.9	6.9	2.2	3.1	2.5	12.6
P	43.6	87.2	87.2	130.8	43.6	43.6	43.6	43.6	87.2
Hf	0.7	1	0.8	7.4	1.2	1.1	3.4	0.7	4.3
Zr	64	70	103	86	44	43	138	28	175
Sm	0.43	0.83	0.31	3.54	1.05	0.44	0.72	0.32	1.64
Ti	119.8	179.7	119.8	778.7	179.7	179.7	299.5	179.7	419.3
Tb	0.04	0.06	0.03	0.4	0.1	0.05	0.1	0.05	0.18
Y	1.7	2	1.3	11.6	3.4	2.1	3.8	1.9	5.1
Tm	0.02	0.03	0.03	0.21	0.06	0.03	0.06	0.04	0.08
Yb	0.26	0.3	0.11	1.36	0.31	0.35	0.48	0.22	0.71
Sc	0.75	0.5	1	1	1.5	1	1.25	1.5	2.25
Cs	0.09	0.08	0.05	1.33	0.28	0.11	0.16	0.09	0.2
Dy	0.32	0.29	0.31	2.44	0.61	0.36	0.26	0.59	0.33
Er	0.18	0.2	0.24	1.17	0.4	0.3	0.18	0.2	0.24
Eu	0.1	0.11	0.11	0.63	0.21	0.1	0.14	0.09	0.24
Ga	0.8	0.9	0.5	5.1	1.4	0.9			
Gd	0.23	0.48	0.36	2.62	0.81	0.42	0.61	0.38	1.04
Ho	0.06	0.07	0.05	0.43	0.17	0.09	0.06	0.07	0.05
Cr	80	30	50	30	30	40	10	10	10
Lu	0.02	0.04	0.03	0.19	0.05	0.04	0.07	0.03	0.1
Pr	0.59	1.28	0.54	5.53	1.68	0.66	0.59	1.28	0.54
V	6	11	7	11	8	8	5	5	5
	DK17	DK18	DK19	DK20	DK21	DK22	DK23	DK24	DK25
wt %					Quartzite				
SiO_2	98.14	82.07	84.9	97.61	88.75	88.01	97.51	88.39	97.05
TiO_2	0.03	0.42	2.37	0.03	0.16	0.13	0.03	0.28	0.05
Al_2O_3	0.39	7.98	5.77	0.46	6.11	5.81	0.58	5.27	1.08
Fe_2O_3	1.04	2.65	2.36	1.07	1.28	2.37	0.97	1.99	0.74
MnO	0.01	0.02	0.02	0.01	0.01	0.02	0.01	0.02	0.01
MgO	0.03	0.16	0.24	0.03	0.09	0.15	0.03	0.13	0.05

(*Continued*)

https://doi.org/10.1017/S001675682400027X

Table 3. (*Continued*)

	DK17	DK18	DK19	DK20	DK21	DK22	DK23	DK24	DK25
CaO	0.01	0.07	0.07	0.01	0.04	0.03	0.01	0.03	0.01
Na_2O	0.02	0.08	0.06	0.02	0.06	0.05	0.01	0.06	0.02
K_2O	0.12	3.24	1.94	0.13	2.24	2.2	0.19	2.32	0.24
P_2O_5	0.005	0.068	0.072	0.008	0.023	0.082	0.009	0.042	0.009
LOI	0.02	1.34	1.26	0.04	1.08	1.09	0.02	0.84	0.29
Total	99.78	98.15	99.11	99.43	99.89	100	99.37	99.43	99.56
Na_2O/K_2O	0.2	0.0	0.0	0.2	0.0	0.0	0.1	0.0	0.1
SiO_2/Al_2O_3	251.6	10.3	14.7	212.2	14.5	15.1	168.1	16.8	89.9
Al_2O_3/TiO_2	13	19	2	15	38	45	19	19	22
CIA	63	60	64	65	63	62	64	58	72
CIW	90	97	97	92	98	98	95	98	96
ppm									
Rb	3	88	58	3.9	59.3	60.9	5.4	61.8	7.4
Ba	46.6	391	319	15.2	266	718	25.8	470	51
Th	0.75	13.45	42.3	1.18	5.26	6.83	0.92	7.86	1.06
U	0.31	2.28	6.97	0.36	0.79	0.91	0.35	1.35	0.37
K	996	26892	16102	1079	18592	18260	1577	19256	1992
Nb	0.9	8.4	43	1	3.7	2.7	0.8	5.6	1.1
Ta	0.1	0.6	3.6	0.1	0.3	0.2	0.1	0.4	0.1
La	2.7	31.6	74	59	13.7	17.4	5.8	16.8	4.7
Ce	5.6	71	158	9.2	33.5	37.3	12.4	36.8	6.6
Sr	4.9	42.8	36.4	5.3	23	25	7.4	31.7	4.5
Nd	2.1	33.8	63.1	3.9	15	18.3	4.7	17.5	2.8
P	21.8	296.48	313.92	34.88	100.28	357.52	39.24	183.12	39.24
Hf	1.5	9.5	58.9	1.6	3.5	3.9	0.8	5.3	1.5
Zr	57	360	2370	59	124	142	35	199	61
Sm	0.41	6.45	12.55	0.74	2.73	3.24	0.65	3.28	0.46
Ti	179.7	2515.8	14196.3	179.7	958.4	778.7	179.7	1677.2	299.5
Tb	0.06	0.81	1.88	0.09	0.32	0.43	0.07	0.49	0.07
Y	2.1	27.4	61.7	2.6	12.5	11.2	1.7	17.6	2.4
Tm	0.04	0.44	1.18	0.03	0.21	0.19	0.04	0.28	0.04
Yb	0.21	3.01	8.28	0.26	1.54	1.15	0.2	2.02	0.3
Sc	1	1.5	2	1.5	1.5	1.75	2.25	1.5	1.5
Cs	0.02	1.06	0.64	0.03	0.56	0.56	0.09	0.64	0.06
Dy	0.36	4.79	11.05	0.44	2.28	2.25	0.26	3.1	0.39
Er	0.18	3.12	7.63	0.29	1.42	1.18	0.21	2.01	0.26
Eu	0.05	1	1.91	0.15	0.56	0.67	0.1	0.7	0.08
Ga	1	9.6	7.1	0.9	6.2	6.3	1	5.9	1.7
Gd	0.4	5.26	11.05	0.63	2.14	3.01	0.43	3.33	0.38
Ho	0.08	0.97	2.22	0.08	0.46	0.44	0.06	0.66	0.1
Cr	30	30	50	10	20	20	10	20	20
Lu	0.04	0.47	1.31	0.05	0.22	0.19	0.03	0.3	0.05
Pr	0.65	8.7	16.6	1.04	3.94	4.5	1.29	4.46	0.74
V	5	24	35	5	16	17	5	13	5

https://doi.org/10.1017/S001675682400027X

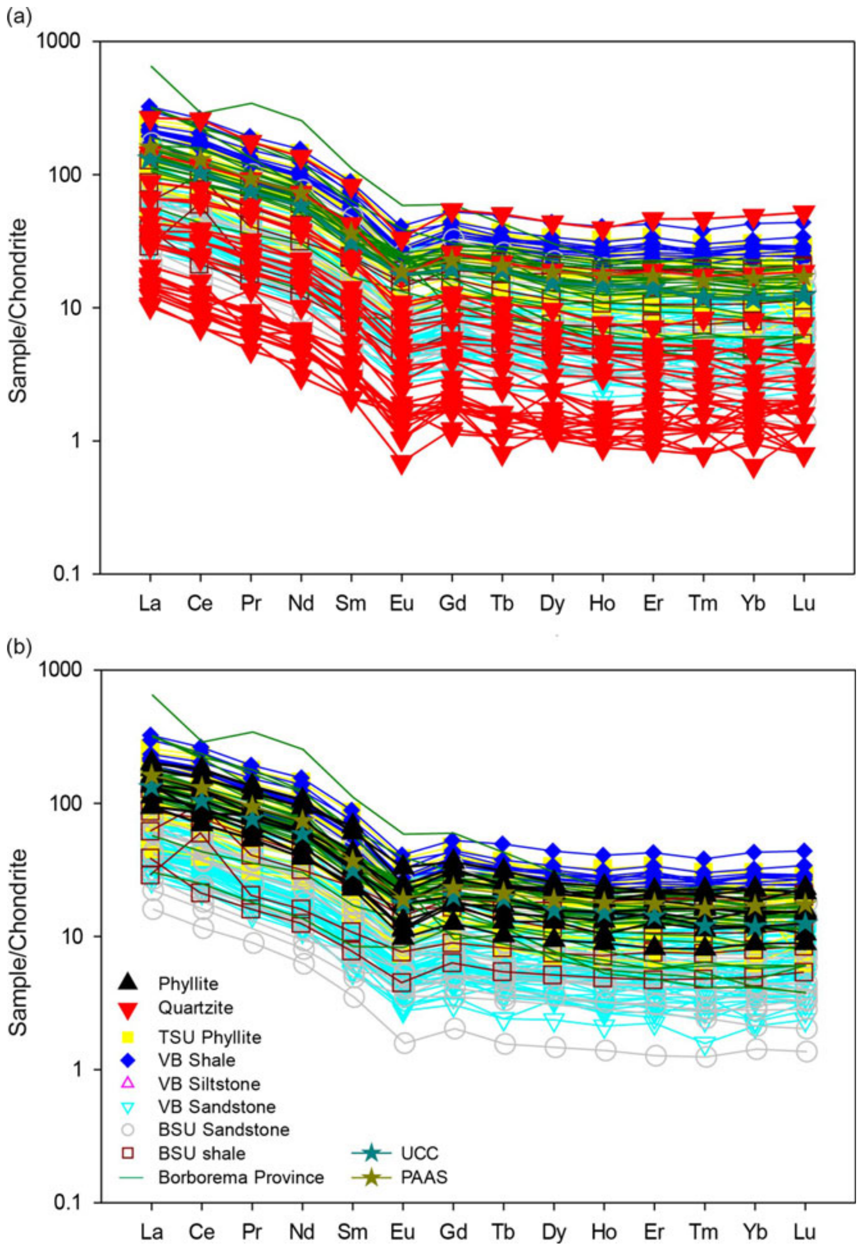

Figure 8. Chondrite-normalized REE plot for the rocks of the TSU (a) quartzites, (b) phyllites. The TSU data are compared to published data from the sandstones and shales of the Buem structural unit, Kwahu-Bombouaka Group of the Voltaian Supergroup and phyllites from the TSU (Osae *et al.*, 2006; Kalsbeek and Frei, 2010; Abu and Zongo, 2017; Anani *et al.*, 2017; 2019; Amedjoe *et al.*, 2018; Abu *et al.*, 2020). Normalizing values for UCC from Rudnick and Gao (2003) and Chondrite from Palme and O'Niel (2014). PAAS is from McLennan (1989).

rocks of the TSU. Figure 11a is a plot of the Q–F–L proposed by Dickinson *et al.* (1983) for depositional setting discrimination. The studied quartzites of the TSU plot mainly in the craton interior, with two samples plotting in the recycled orogen and one sample in the transitional continent (Fig. 11a). Continental blocks represent sediments that originated from stable craton interiors or the uplift of basement rocks. Sedimentary rocks from this setting are generally quartz arenites with subordinate arkosic sandstone, as in the case of the rocks of the TSU (Dickinson *et al.*, 1983). The two samples that plot in the recycled orogen are those that originated from sedimentary strata and volcanic/plutonic rocks or metamorphic equivalent that are eroded as a result of uplift during an orogenic event of fold-and-thrust belts (Dickinson *et al.*, 1983). Sedimentary rocks formed here are feldspar-poor and lithic fragment-rich; in the case of the TSU, they are sublitharenite (Fig. 6; Dickinson *et al.*, 1983).

The studied rocks of the TSU again plot dominantly in the passive margin field with few plotting in the active margin field on the DF(A-P)m tectonic discrimination diagram (Fig. 11b) after Verma and Armstrong-Altrin (2016). In order to better understand the tectonic environment of the TSU, a Th–Sc–Zr/10 immobile trace elements discrimination diagram by Bhatia & Crook (1986) was plotted. This diagram is helpful in distinguishing between four distinct tectonic settings: Passive Margins, Active Continental Margins, Continental Island Arcs and Oceanic Island Arcs. The TSU samples dominantly plot in

https://doi.org/10.1017/S001675682400027X

Table 4. Elemental ratios of the rocks of the TSU compared with sediments derived from felsic and mafic rocks

	Quartzite	Phyllite	TSU Phyllite*	VB Shale*	VB Siltstone*	VB Sandstone	BSU Sandstone*	BSU Shale*	Range of sediments from felsic sources	Range of sediments from mafic sources
La/Sc	1.4–31.4	3.1–33.4	1.9–6.5	2.3–4.7	1.7–11.8	3.1–8.3	1.7–12.1	0.5–0.9	2.50–16.3	0.43–0.86
Th/Sc	2.0–10.0	0.30–28.0	0.9–1.5	0.8–1.6	0.7–3.7	0.7–6.5	0.3–2.3	0.1–0.7	0.84–20.5	0.05–0.22
Eu/Eu*	0.52–0.75	0.38–1.01	0.46–0.68	0.54–0.66	0.54–0.73	0.50–1.31	0.66–1.09	0.62–0.74	0.40–0.94	0.71–0.95
(La/Lu)N	5.93–13.86	0.26–27.7	4.54–10.86	7.39–8.77	0.13–17.03	1.24–21.51	3.62–21.01	3.06–7.60	3.00–27.0	1.10–7.00

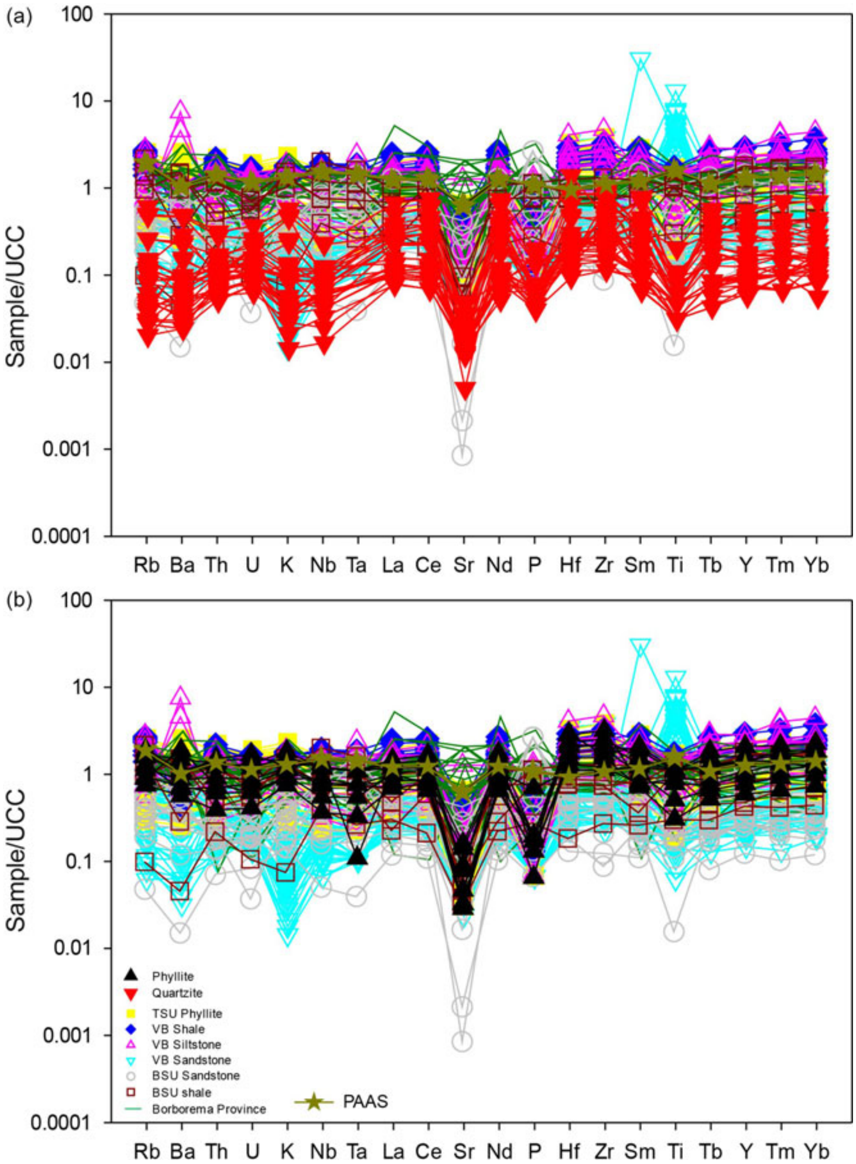

Figure 9. Multi-elements plot normalized to UCC for the rocks of the TSU (a) quartzites, (b) phyllites. The TSU data are compared to published data from the sandstones and shales of the Buem structural unit, Kwahu-Bombouaka Group of the Voltaian Supergroup and phyllites from the TSU (Osae *et al.*, 2006; Kalsbeek and Frei, 2010; Abu and Zongo, 2017; Anani *et al.*, 2017; 2019; Amedjoe *et al.*, 2018; Abu *et al.*, 2020). Normalizing values for UCC from Rudnick and Gao (2003) and Chondrite from Palme and O'Niel (2014). PAAS is from McLennan (1989).

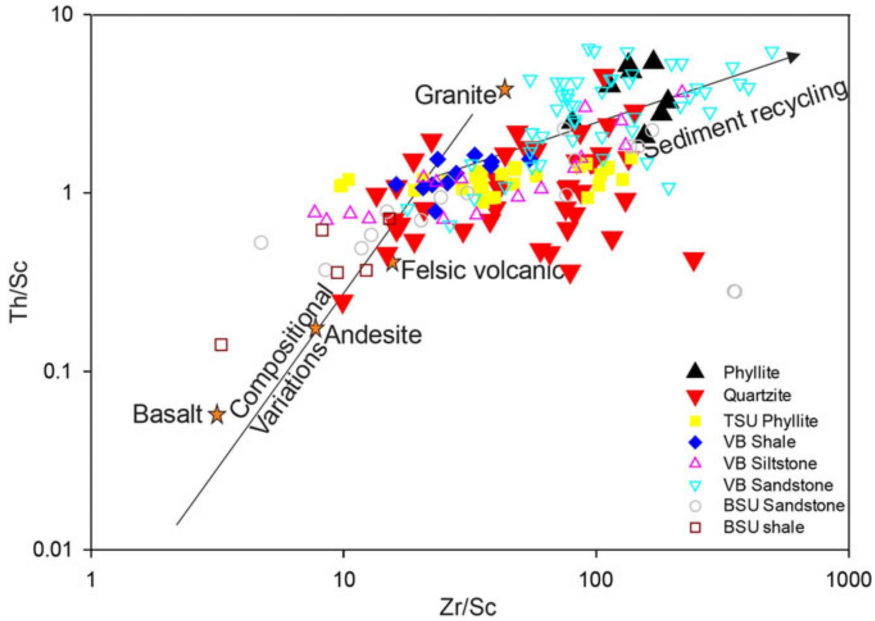

Figure 10. (a) Th/Sc versus Zr/Sc after (McLennan *et al.*, 1993). Note that data points from TTG, granite, felsic volcanic rocks, andesite and basalt are from Condie (1993) The TSU data are compared to published data from the sandstones and shales of the Buem structural unit, Kwahu-Bombouaka Group of the Voltaian Supergroup and phyllites from the TSU (Osae *et al.*, 2006; Kalsbeek and Frei, 2010; Abu and Zongo, 2017; Anani *et al.*, 2017, 2019; Amedjoe *et al.*, 2018; Abu *et al.*, 2020).

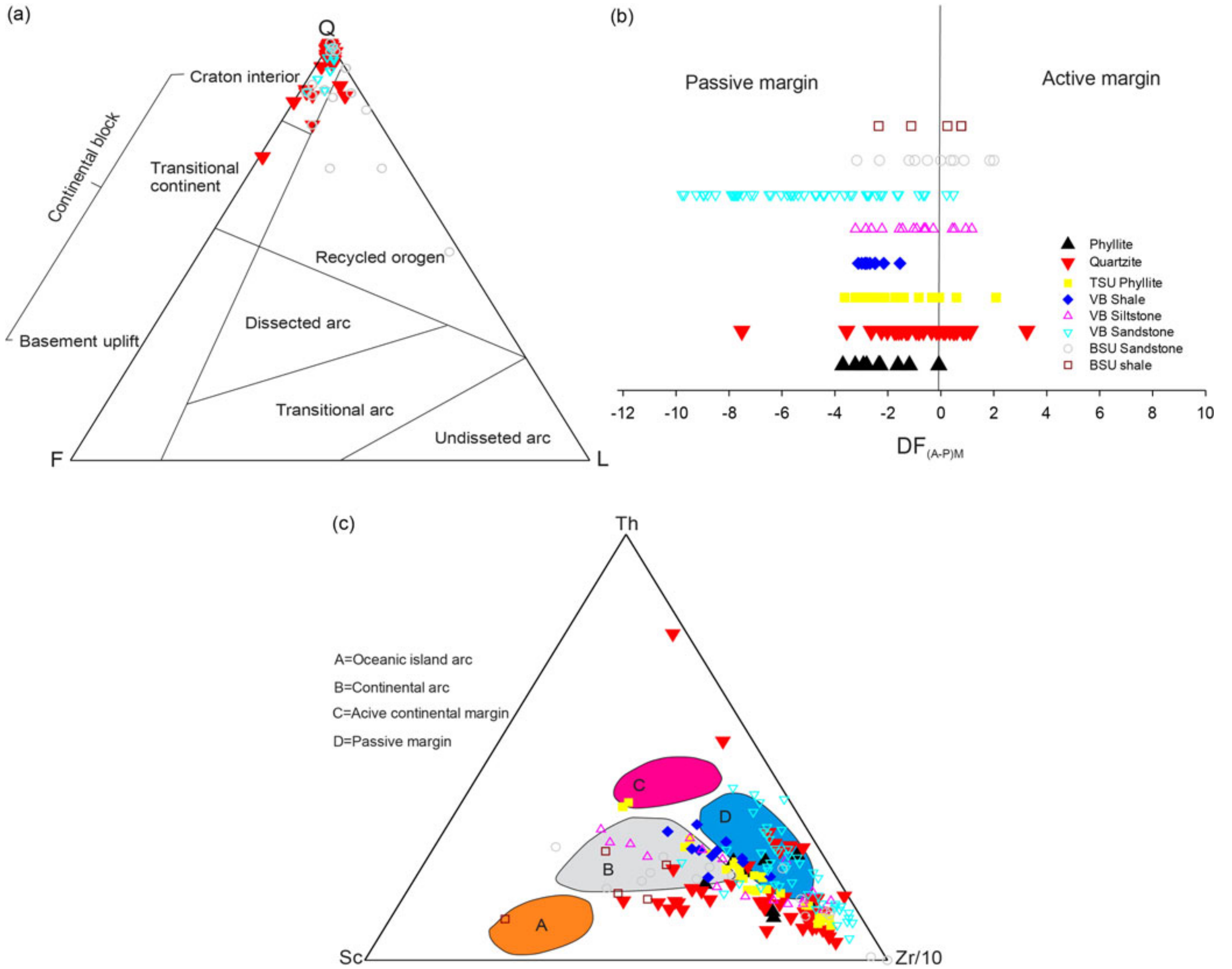

Figure 11. Tectonic setting discrimination diagrams for the rocks of the TSU (a) Q–F–L diagram (Dickinson *et al.*, 1983), (b) DF(A-P)M diagram (after Verma and Armstrong-Altrin, 2016) and (c) Th–Sc–Zr/10 plot (Bhatia and Crook, 1986). The TSU data are compared to published data from the sandstones and shales of the Buem structural unit, Kwahu-Bombouaka Group of the Voltaian Supergroup and phyllites from the TSU (Osae *et al.*, 2006; Kalsbeek and Frei, 2010; Abu and Zongo, 2017; Anani *et al.*, 2017, 2019; Amedjoe *et al.*, 2018; Abu *et al.*, 2020). DF = Discriminant function, A and P are active and passive margin, respectively, and M = major element composition.

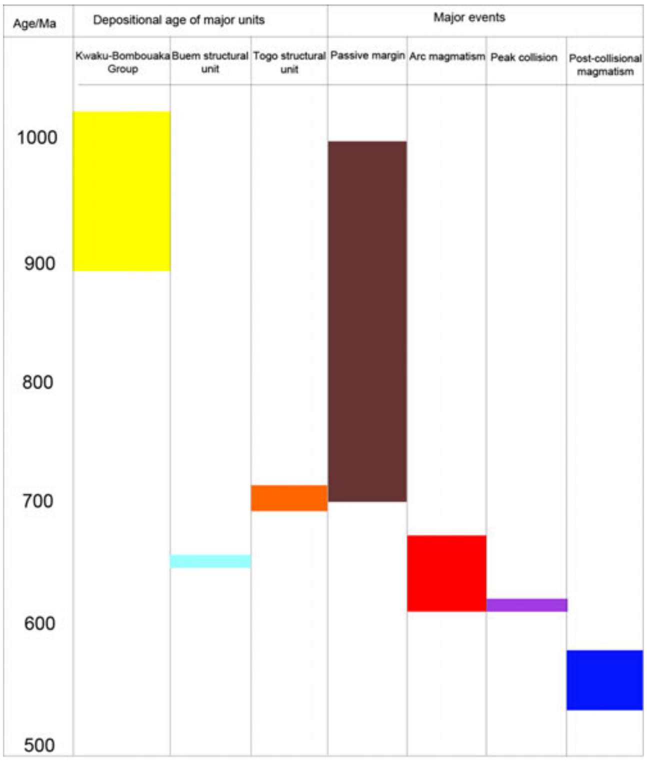

Figure 12. Space–time plot showing the age range of principal rock units and major events of the Dahomeyide belt. Published age data are from Clauer (1976), Clauer *et al.* (1982), Ganade de Araujo *et al.* (2014b) and Ganade de Araujo *et al.* (2016).

and around the passive margin setting, with some samples falling in and around the active continental margin and continental arc settings (Fig. 11c). Overall, the mineralogical, major and trace element compositions of the rocks of the TSU suggest dominantly passive margin affinity with subordinate active margin signature.

Prior to the Pan-African convergence, there was a rifting formation and evolution of a passive margin basin at *c.* 1000 and 700 Ma (Ganade de Araujo *et al.*, 2016; Caxito *et al.*, 2020; Kwayisi *et al.*, 2022b). The depositional age of the rocks of the TSU is poorly constrained at *c.* 703±8 Ma (U-Pb zircon age metabasaltic rock), and this age falls within the age of passive margin formation (1000 – 700 Ma; Fig. 12; Ganade de Araujo *et al.*, 2016). Again, Kalsbeek *et al.* (2008) inferred a passive margin setting for the quartzites of the TSU because of the presence of the youngest detrital zircon ages of >900 Ma. This interpretation is, however, inconsistent with the active margin signature exhibited by some of the rocks of the TSU from geochemistry. Thus, the TSU might have received sediments during the pre-convergence (i.e. rifting and passive margin) phase and later during the convergence (subduction and collisional) phase of the Pan-African orogeny. This inference needs to be tested from detailed geochronological studies, as the convergence phase would introduce detrital zircons of ages between 700 and 550 Ma (Fig. 12).

3.e. Formation and evolution of passive margin sequences of the Pan-African Dahomeyide belt

Many researchers have proposed the formation of TSU rocks in the same depositional setting and similar provenance as the other siliciclastic rocks of the Dahomeyide belt external nappes zone (Buem structural unit and the Kwahu-Bombuaka Group (e.g., Affaton, 1990; Anani *et al.*, 2019; Kwayisi *et al.*, 2022b). This interpretation is based on similar U-Pb zircon age populations obtained for these units (Kalsbeek *et al.*, 2008; Kwayisi *et al.*, 2022b). The TSU, Kwahu-Bombuaka Group and the Buem structural unit have zircon age populations in the range 930 – 2200 Ma, 1130 – 2200 Ma and 970 – 2200 Ma, respectively, with significant Archean zircon grains (Kwayisi *et al.*, 2022b). The presence of the youngest detrital zircon ages older than 900 Ma is an indication of the deposition of these units in a passive margin depositional setting (Kwayisi *et al.*, 2022b).

Two major passive margin sequences have been identified from the detrital zircon age populations. (i) lower passive margin sequences with ages dominantly between 1800 and 2200 Ma, which lack Neoproterozoic detrital zircons and (ii) upper passive margin sequences with significant Neoproterozoic detrital zircons between 900 and 1000 Ma (Kwayisi *et al.*, 2022b). Nonetheless, similarities in zircon age population among units could mean one of the following:

i. the units have been deposited at the same time, sampling the same sources (basement rock or older sediments), or
ii. the units have been deposited at different times but have sampled the same sources or unrelated sources with similar zircon age distributions, or
iii. the units are of different ages, the younger formed by recycling of the older (Andersen *et al.*, 2019).

In this study, petrographic investigations have revealed that the quartzites of the TSU formed probably in a passive margin depositional setting akin to the sandstones of the Buem structural unit and the Kwahu-Bombouaka Group (Fig. 11a). Major and trace element composition suggests that the sediments of the TSU were sourced from the same source area and deposited in the same depositional setting as the Buem structural unit and Kwahu-Bombouaka Group. The three units depict similar REE and trace element patterns on the Chondrite- and UCC-normalized diagrams (Figs. 8 and 9). Provenance and depositional setting indicators suggest dominantly passive margin deposition for the TSU's rocks formed with the sediments derived from intermediate and felsic sources. These provenance and depositional setting patterns have also been identified in the Buem structural unit and the Kwahu-Bombouaka Group (Figs. 11b and 11c; Table 1). The Kwahu-Bombouaka Group was deposited earlier (deposition age = 959±65 Ma, Rb-Sr isochron age) than the TSU (depositional age = 703 ± 8 Ma, U-Pb zircon age) and the Buem structural unit (Rb-Sr of 650 Ma; Fig. 12; Table 1). The large variation in depositional ages indicates a long period of passive margin formation, from 1000 to 700 Ma. This age corresponds to the break-up of Rodinia supercontinent (Evans, 2009, 2013).

The structural architecture and deformational history of the TSU are similar to the Buem structural unit and the eastern margin of the Voltaian Supergroup. In this study, three deformational (D1 – D3) events have been identified in the rocks of the TSUs. The main deformational event (D2) expressed as NNW-striking S2 foliation, isoclinal folds with an N-plunging fold axis and downdip stretching lineation is similar to the main D2 event in the Buem structural unit (Kwayisi *et al.*, 2020). This D2 event corresponds to an E-W shortening at 640 – 620 Ma during the convergence phase of the Pan-African orogeny (Kwayisi *et al.*, 2020). Thus, the similarities in deformation style, petrographic and geochemical signatures could mean that the three were deposited within the

https://doi.org/10.1017/S001675682400027X

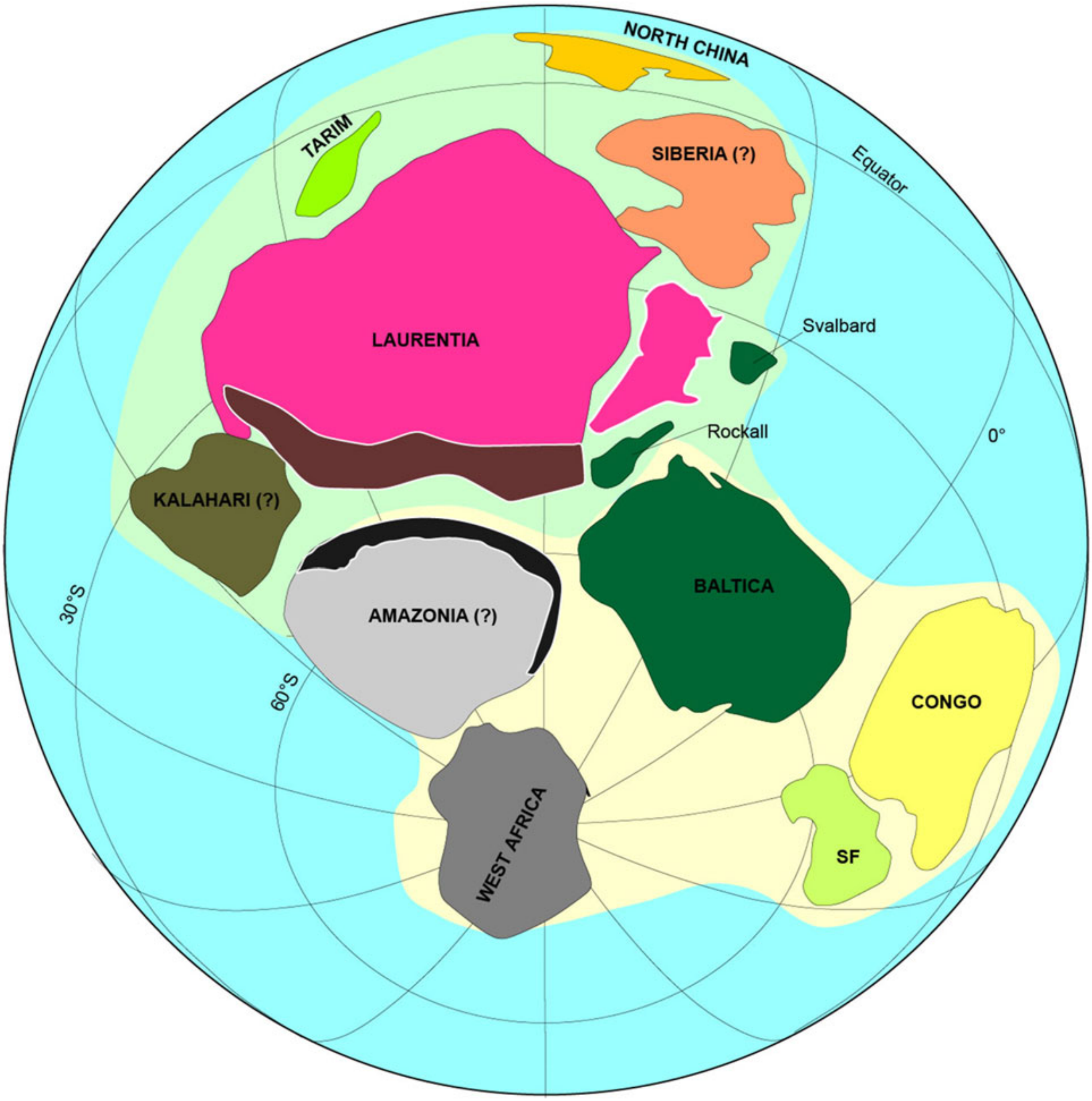

Figure 13. The palaeogeography reconstruction of Rodinia (modified after Antonia *et al.* 2021), which suggests that during Rodinia time, the WAC and the Amazonian Craton were likely not separated by any major seas. It is postulated that these cratons may have been connected from the Paleoproterozoic era until the break-up of Pangea.

same depositional basin, sampling the same source area lithology and later deformed by the Pan-African orogeny. Hence, during the break-up Rodinia and prior to the assembly of Gondwana supercontinents, there was the formation of a passive margin basin that was later tectonically deformed and metamorphosed during the Pan-African orogeny at the eastern margin of the West African Craton. Available detrital zircon age data suggest that abundant Mesoproterozoic detrital zircon (1600 – 1000 Ma; Kalsbeek *et al.*, 2008; Ganade de Araujo *et al.*, 2016; Kwayisi *et al.*, 2022b) grains are recorded for the passive margin sequences of the Dahomeyide belt. No record of Mesoproterozoic granitoid and granitic gneisses on the WAC suggests sediment provenance from the Amazonia Craton. This finding thus supports the fact that the West African–Amazonian cratons coexisted without any major oceans separating them during the Rodinia Period (Fig. 13; Kalsbeek *et al.*, 2008; Kwayisi *et al.*, 2022b).

4. Conclusion

The framework grains of the quartzites of the TSU, which consist of dominant quartz, minor feldspar and lithic fragments, suggest they are quartz arenite, subarkose and sublitharenite. This classification is comparable to the siliciclastic rocks of the Kwahu-Bombouaka Group of the Voltaian Supergroup and Buem structural unit. On the whole, the studied rocks show similar REE and multi-element patterns on the chondrite and UCC normalized diagram that indicate the derivation of the sediments from similar sources. The presence of abundant quartz grains coupled with the $(La/Lu)_N$, Th/Sc, La/Sc, La/Co and Th/Co values suggest mature sediments sourced from intermediate to felsic source area lithology. Provenance and depositional indicators of the studied rocks of the TSU resemble those of the siliciclastic rocks of the Kwahu-Bombouaka Group and Buem structural unit. Available petrographic, geochemical and geochronological data of the Buem structural unit and Voltaian Supergroup indicate deposition in a passive margin setting with sediment sourced from the Amazonian and West African cratons, and this is akin to the TSU. Therefore, the TSU was deposited in a passive margin setting with the Amazonian and West African cratons as potential provenance. Passive margin formation is dated between 1000 and 700 Ma, corresponding to the break-up of the supercontinent Rodinia. The structural architecture and deformational history of the TSU are similar to those of the Buem structural unit and the eastern margin of the Voltaian Supergroup. Thus, a Neoproterozoic passive margin basin formed and was deformed and metamorphosed during the break-up of Rodinia and prior to the assembly of Gondwana supercontinents. Hence, the West African–Amazonian cratons coexisted without any major oceans separating them during the Rodinia Period.

Acknowledgments. The authors acknowledge the financial support provided by the Department of Earth Science, College of Basic and Applied Sciences (CBAS), University of Ghana.

References

Abu M, Sunkari ED and Gürel A (2020) Paleocurrent analysis, petrographic, geochemical and statistical appraisal of Neoproterozoic siliciclastic sediments, NE Voltaian Basin, Ghana: a multidisciplinary approach to paleogeographic reconstruction. *Journal of Sedimentary Environments* **5**, 199–218.

Abu M and Zango MS (2017) Geochemical characteristics of the Neoproterozoic Anyaboni sandstone of the southeastern Voltaian Basin, Ghana. *Scientific Research Journal* **5**, 54–65.

Adjei AO and Tetteh GM (1997) Deformational phases of the Togo series, Ho-Nyive-Honuta area, Ghana. *Ghana Mining J.* **3**, 1–9.

Affaton P (1990) Le bassin des Volta (Afrique de l'Ouest): une marge passive, d'âge protérozoïque supérieur, tectonisée au Panafricain (600 plus ou moins 50 Ma). Thèse Doctorat d'Etat, collections Etude et Thèse, ORSTOMS, Paris, 499.

Affaton P, Aguirre, L and Ménot RP (1997) Thermal and geodynamic setting of the Buem volcanic rocks near Tiélé, Northwest Bénin, West Africa. *Precambrian Research* **82**, 191–209.

Affaton P, Kröner, A and Seddoh KF (2000) Pan-African granulite formation in the Kabye Massif of northern Togo (West Africa): Pb– Pb zircon ages. *International Journal of Earth Science* **88**, 778–90.

Agbossoumondé Y, Guillot, S and Ménot RP (2004) Pan-African subduction–collision event evidenced by high-P coronas in metanorites from the Agou massif (southern Togo). *Precambrian Research* **135**, 1–21.

Agbossoumondé Y, Menot RP and Guillot S (2001) Metamorphic evolution of Neoproterozoic eclogites from south Togo (West Africa). *Journal of African Earth Sciences* **33**, 227–44.

Agyei Duodu J, Loh GK, Hirdes W, Boamah KO, Baba M, Anokwa YM, Asare C, Brako-hiapa E, Mensah RB, Okla R, Toloczyki M, Davis DW and Glück S (2009). Geological Map of Ghana 1:1 000 000. BGS/GGS, Accra, Ghana/Hannover,Germany.

Aidoo F, Nude PM, Dampare SB, Agbossoumond Y, Salifu M, Appenteng MK and Tulasi, D (2014) Geochemical Characteristics of Granitoids (Ho Gneiss) from the Pan–African Dahomeyide Belt, Southeastern, Ghana: Implications for Petrogenesis and Tectonic Setting. *Journal of Environment and Earth Science* **4**, 46–65.

Aidoo F, Sun FY, Liang, T and Nude PM (2020) New insight into the Dahomeyide Belt of southeastern Ghana, West Africa: Evidence of arc-continental collision and Neoarchaean crustal reworking. *Precambrian Research* **347**, 105836.

Alayi G, Kpanzou SA. M, Agbossoumondé Y, Padaro E, Menot RP and Tairou MS (2023) Petrology, Age and Geodynamic Implication of the Panafrican Granitoids Associated with the Glito-Kpatala Shear Zone (South-East Togo). *International Journal of Geosciences* **14**, 1193–225.

Amedjoe CG, Gawu SK. Y, Ali B, Aseidu, DK and Nude, PM (2018) Geochemical compositions of Neoproterozoic to Lower Palaeozoic (?) shales and siltstones in the Volta Basin (Ghana): Constraints on provenance and tectonic setting. *Sedimentary Geology* **368**, 114–31.

Amponsah, PO, Kwayisi D, Awunyo EK, Sapah MS, Sakyi PA, Su BX, . . . and Nude PM (2023) New evidence for crustal reworking and juvenile arc-magmatism during the Palaeoproterozoic Eburnean events in the Suhum Basin, South-east Ghana. *Geological Journal* **58**, 3734–55.

Anani C (1999) Sandstone petrology and provenance of the Neoproterozoic Voltaian Group in the southeastern Voltaian Basin, Ghana. *Sedimentary Geology* **128**, 83–98.

Anani C, Modupe M, David A, Jacob K, Daniel A and Boamah D (2013) Geochemistry and provenance of sandstones from Anyaboni and surrounding areas in the Voltaian basin, Ghana. *International Research Journal of Geology and Mining* **3**, 206–12.

Anani CY, Bonsu S, Kwayisi D and Asiedu DK (2019). Geochemistry and provenance of Neoproterozoic metasedimentary rocks from the TSU, Southeastern Ghana. *Journal of African Earth Sciences* **153**, 208–18.

Anani CY, Mahamuda A, Kwayisi D and Asiedu DK (2017). Provenance of sandstones from the Neoproterozoic Bombouaka Group of the volta Basin, northeastern Ghana. *Arabian Journal of Geosciences***10**, 465.

Andersen T, Elburg MA and Van Niekerk HS (2019) Detrital zircon in sandstones from the Palaeoproterozoic Waterberg and Nylstroom basins, South Africa: Provenance and recycling. *South African Journal of Geology* **122**, 79–96.

Anum S, Sakyi PA, Su BX, Nude PM, Nyame F, Asiedu D and Kwayisi D (2015) Geochemistry and geochronology of granitoids in the Kibi-Asamankese area of the Kibi-Winneba volcanic belt, southern Ghana. *Journal of African Earth Sciences* **102**, 166–179.

Armstrong-Altrin JS (2009) Provenance of sands from Cazones, Acapulco, and Bahía Kino beaches, Mexico. *Revista Mexicana de Ciencias Geológicas* **26**, 764–82.

Armstrong-Altrin JS (2015) Evaluation of two multidimensional discrimination diagrams from beach and deep-sea sediments from the Gulf of Mexico and their application to Precambrian clastic sedimentary rocks. *International Geology Review* **57**, 1446–61.

Armstrong-Altrin, JS, Nagarajan, R, Balaram, V and Natalhy-Pineda, O (2015) Petrography and geochemistry of sands from the Chachalacas and Veracruz beach areas, western Gulf of Mexico, Mexico: constraints on provenance and tectonic setting. *Journal of South American Earth Sciences* **64**, 199–216.

Asiedu DK, Asong S, Atta-Peters D, Sakyi PA, Su BX, Dampare SB and Anani CY (2017) Geochemical and Nd-Isotopic compositions of juvenile-type Paleoproterozoic Birimian sedimentary rocks from southeastern West African Craton (Ghana): Constraints on provenance and tectonic setting. *Precambrian Research* **300**, 40–52.

Attoh K (1998) High-pressure granulite facies metamorphism in the Pan-African Dahomeyide Orogen, West Africa. *Journal of Geology* **106**, 236–46.

Attoh K, Corfu, F and Nude PM (2007) U-Pb zircon age of deformed carbonatite and alkaline rocks in the Pan-African Dahomeyide suture zone, West Africa. *Precambrian Research* **155**, 251–60.

Attoh K, Dallmeyer RD and Affaton P (1997) Chronology of nappe assembly in the Pan-African Dahomeyide Orogen, West Africa: evidence from ^{40}Ar-^{39}Ar mineral ages. *Precambrian Research* **82**, 153–71.

Attoh K, Hawkings G and Bowring SA (1991) U–Pb zircon ages from the Pan-African Dahomeyide Orogen, West Africa. EOS Trans. *Am. Geophys. Union Spring Meeting*, 72, abstract.

Attoh K and Morgan J (2004) Geochemistry of high-pressure granulites from the Pan-African Dahomeyide orogen, West Africa: constraints on the origin and composition of the lower crust. *Journal of African Earth Sciences* **39**(3-5), 201–208.

Attoh K and Nude PM (2008) Tectonic significance of carbonatite and ultrahigh-pressure rocks in the Pan-African Dahomeyide suture zone, southeastern Ghana. *Geological Society, London, Special Publications* **297**, 217–31.

Attoh K, Samson S, Agbossoumondé Y, Nude PM and Morgan J (2013) Geochemical characteristics and U–Pb zircon LA-ICPMS ages of granitoids from the Pan-African Dahomeyide Orogen, West Africa. *Journal of African Earth Sciences* **79**, 1–9.

Baiyegunhi C, Liu, K and Gwavava O (2017) Geochemistry of sandstones and shales from the Ecca Group, karoo supergroup, in the Eastern Cape Province of South Africa: implications for provenance, weathering and tectonic setting. *Open geosciences* **9**, 340–60.

Barfod GH, Vervoort JD, Montanez IP and Riebold S (2004) Lu-Hf geochronology of phosphates in ancient sediments. 13th Goldschmidt conference, Copenhagen, *Geochim. Cosmochim. Acta*, *abstract, 68*(11), A336.

Bhatia MR and Crook KA (1986) Trace element characteristics of graywackes and tectonic setting discrimination of sedimentary basins. *Contributions to Mineralogy and Petrology* **92**, 181–93.

Bhatia MR and Taylor SR (1981) Trace-element geochemistry and sedimentary provinces: a study from the Tasman Geosyncline, Australia. *Chemical geology* **33**, 115–25.

Carney JN, Jordan CJ, Thomas CW, Condon DJ, Kemp SJ and Duodo JA (2010) Lithostratigraphy, sedimentation and evolution of the Volta Basin in Ghana. *Precambrian Research* **183**, 701–24.

Cawood PA, Hawkesworth CJ and Dhuime B (2012) Detrital zircon record and tectonic setting. *Geology* **40**, 875–78.

Caxito FDA, Santos LCMDL, Ganade CE, Bendaoud A, Fettous EH and Bouyo MH (2020) Toward an integrated model of geological evolution for NE Brazil-NW Africa: The Borborema Province and its connections to the Trans-Saharan (Benino-Nigerian and Tuareg shields) and Central African orogens. *Brazilian Journal of Geology* **50**, e2019122.

Clauer N (1976) Isotopic geochemistry of strontium in sedimentary environments. Application to the geochronology of the cover of the West African craton. *Persée-Portal of scientific j. in SHS* 45, (1).

Clauer N, Caby R, Jeannette D and Trompette R (1982) Geochronology of sedimentary and metasedimentary Precambrian rocks of the West African craton. *Precambrian Research* **18**, 53–71.

Condie KC (1993) Chemical composition and evolution of the upper continental crust: contrasting results from surface samples and shales. *Chemical Geology* **104**, 1–37.

Cordani UG, Teixeira W, D'Agrella-Filho MS and Trindade RI (2009) The position of the Amazonian Craton in supercontinents. *Gondwana Research* **15**, 396–407.

Cullers RL (1994) The controls on the major and trace element variation of shales, siltstones, and sandstones of Pennsylvanian-Permian age from uplifted continental blocks in Colorado to platform sediment in Kansas, USA. *Geochimica et Cosmochimica Acta* **58**, 4955–72.

Cullers RL (2000) The geochemistry of shales, siltstones and sandstones of Pennsylvanian–Permian age, Colorado, USA: implications for provenance and metamorphic studies. *Lithos* **51**, 181–203.

Cullers RL, Basu, A and Suttner LJ (1988) Geochemical signature of provenance in sand-size material in soils and stream sediments near the Tobacco Root batholith, Montana, USA. *Chemical Geology* **70**, 335–48.

Dabard MP (1990) Lower Brioverian formations (Upper Proterozoic) of the Armorican Massif (France): geodynamic evolution of source areas revealed by sandstone petrography and geochemistry. *Sedimentary Geology* **69**, 45–58.

Deynoux M, Affaton P, Trompette, R and Villeneuve, M (2006) Pan-African tectonic evolution and glacial events registered in Neoproterozoic to Cambrian cratonic and foreland basins of West Africa. *Journal of African Earth Sciences* **46**, 397–426.

Dickinson WR (1985) Interpreting provenance relations from detrital modes of sandstones. In *Provenance of arenites*, pp. 333–361. Dordrecht: Springer.

Dickinson WR, Beard LS, Brakenridge GR, Erjavec JL, Ferguson RC, Inman KF, Knepp RA, Lindberg FA and Ryberg PT (1983) Provenance of North American Phanerozoic sandstones in relation to tectonic setting. *Geological Society of America Bulletin* **94**, 222–235.

Duclaux G, Ménot RP, Guillot S, Agbossoumondé Y and Hilairet N (2006) The mafic layered complex of the Kabyé massif (north Togo and north Benin): Evidence of a Pan-African granulitic continental arc root. *Precambrian research*, **151**, 101–18.

Egal E, Thiéblemont D, Lahondere D, Guerrot C, Costea CA, Iliescu D, Delor C, Goujou JC, Lafon JM, Tegyey M and Diaby S (2002) Late Eburnean granitization and tectonics along the western and northwestern margin of the Archean Kénéma–Man domain (Guinea, West African Craton). *Precambrian Research* **117**, 57–84.

Evans DA (2009) The palaeomagnetically viable, long-lived and all-inclusive Rodinia supercontinent reconstruction. *Geological Society, London, Special Publications* **327**, 371–404.

Evans DA (2013) Reconstructing pre-Pangean supercontinents. *Bulletin*, **125**, 1735–51.

Fedo CM, Sircombe KN and Rainbird RH (2003) Detrital zircon analysis of the sedimentary record. *Reviews in Mineralogy and Geochemistry* **53**, 277–303.

Ganade de Araujo CE, Cordani UG, Agbossoumounde Y, Caby R, Basei MA, Weinberg RF and Sato K (2016) Tightening-up NE Brazil and NW Africa connections: New U–Pb/Lu-Hf zircon data of a complete plate tectonic cycle in the Dahomey belt of the West Gondwana Orogen in Togo and Bénin. *Precambrian Research* **276**, 24–42.

Ganade de Araujo CE, Rubatto D, Hermann J, Cordani UG, Caby R and Basei MA (2014a) Ediacaran 2,500-km-long synchronous deep continental subduction in the West Gondwana Orogen. *Nature Communications* **5**, 1–8.

Ganade de Araujo CE, Weinberg RF and Cordani UG (2014b) Extruding the Borborema Province (NE-Brazil): a two-stage Neoproterozoic collision process. *Terra Nova*, **26**(2), 157–168.

Girty GH, Hanson AD, Yoshinobu AS, Knaack C and Johnson D (1994) Provenance of Paleozoic mudstones in a contact metamorphic aureole determined by rare earth element, Th, and Sc analyses, Sierra Nevada, California. *Geology* **21**, 363–66.

Grenholm M, Jessell M and Thébaud N (2019) A geodynamic model for the Paleoproterozoic (ca. 2.27–1.96 Ga) Birimian Orogen of the southern West African Craton–Insights into an evolving accretionary-collisional orogenic system. *Earth-Science Reviews*. **192**, 138–93.

Guillot S, Agbossoumondé Y, Bascou J, Berger J, Duclaux G, Hilairet N, Ménot R and Schwartz S (2019) Transition from subduction to collision recorded in the Pan-African arc complexes (Mali to Ghana). *Precambrian Research* **320**, 261–80.

Jiang YD, Schulmann K, Kröner A, Sun M, Lexa O, Janoušek V, Buriánek D, Yuan C and Hanžl P (2017) Neoproterozoic-Early Paleozoic Peri-Pacific Accretionary Evolution of the Mongolian College System: Insights From Geochemical and U-Pb Zircon Data From the Ordovician Sedimentary Wedge in the Mongolian Altai. *Tectonics* **36**, 2305–31.

Junner N (1935) *Gold in Gold Coast*. Accra, Ghana: Geological Survey Department.

Kalsbeek, F, Affaton, P, Ekwueme, B, Frei, R and Thrane K (2012) Geochronology of granitoid and metasedimentary rocks from Togo and Bénin, West Africa: comparisons with NE Brazil. *Precambrian Research* **196**, 218–33.

Kalsbeek F, Frei D and Affaton P (2008) Constraints on provenance, stratigraphic correlation and structural context of the Volta basin, Ghana, from detrital zircon geochronology: An Amazonian connection?. *Sedimentary Geology* **212**), 86–95.

Kalsbeek F, Frei D, Schersten A, Frei R, Gerdes A and Kalvig P (2020) Enigmatic 1146±4 Ma old granite in the southeastern rim of the West African craton, now part of the Dahomeyan orogenic belt in Ghana. *Journal of African Earth Sciences*, **167**, 103814.

Kalsbeek F and Frei R (2010) Geochemistry of Precambrian sedimentary rocks used to solve stratigraphical problems: an example from the Neoproterozoic Volta basin, Ghana. *Precambrian Research* **176**, 65–76.

Kazapoe RW, Okunlola O, Arhin E, Olisa O, Harris C, Kwayisi D, Torkorno S and Amuah EE. Y (2022). Geology and Isotope Systematics of Gold Deposits in the Abansuoso Area of the Sefwi Belt, Southwestern Ghana. *Geology, Ecology, and Landscapes* **8**, 423–444.

Kazapoe RW, Okunlola O, Arhin E, Olisa O, Kwayisi D, Dzikunoo EA and Amuah EE. Y (2023). Compositional characteristics of mineralised and

https://doi.org/10.1017/S001675682400027X

unmineralised gneisses and schist around the Abansuoso area, southwestern Ghana. *Applied Earth Science* **132**, 36–51

Kesse GO (1985) *The Mineral and Rock Resources of Ghana*. Rotterdam/Boston: Balkema.

Kouamelan AN, Delor C and Peucat JJ (1997) Geochronological evidence for reworking of Archean terrains during the early Proterozoic (2.1 Ga) in the western Cote d'Ivoire (Man Rise-West African Craton). *Precambrian Research* **86**, 177–99.

Kwayisi D, Agra NA, Dampare SB, Asiedu DK, Amponsah PO and Nude PM (2017) Two suites of gabbros in the Buem Structural Unit, of the Pan-African Dahomeyide orogen, southeastern Ghana: Constraints from new field and geochemical data. *Journal of African Earth Sciences* **129**, 45–55.

Kwayisi D, Elburg M and Lehmann J (2022a) Preserved ancient oceanic lithosphere within the Buem structural unit at the eastern margin of the West African Craton. *Lithos* **410**, 106585.

Kwayisi D, Lehmann J and Elburg M (2020) The architecture of the Buem Structural Unit: Implications for the tectonic evolution of the Pan-African Dahomeyide Orogen, West Africa. *Precambrian Research* **338**, 105568.

Kwayisi D, Lehmann J and Elburg M (2022b) Provenance and depositional setting of the Buem structural unit (Ghana): Implications for the paleogeographic reconstruction of the West African and Amazonian cratons in Rodinia. *Gondwana Research* **109**, 183–204.

Kwayisi D, Nyavor E, Dzikunoo EA, Fynn IEM, Kutu J and Nude PM (2023) Cryogenian-Ediacaran crustal growth and evolution of the active margin of the Dahomeyide belt, Ghana. *Geological Magazine* **160**, 1914–1931.

Lafon JM, Delor C, Guerrot C and Lahondère D (2003) Archean crustal remnants in the easternmost part of the Guiana Shield: Pb-Pb and Sm-Nd geochronological evidence for Mesoarchean versus Neoarchean signatures. *Geologie de la France* **2-3-4**, 83–99.

Ledru P, Johan V, Milési JP and Tegyey M (1994) Markers of the last stages of the Palaeoproterozoic collision: evidence for a 2 Ga continent involving circum-South Atlantic provinces. *Precambrian Research* **69**, 169–91.

McLennan SM (1989) Rare earth elements in sedimentary rocks: influence of provenance and sedimentary processes. *Geochemistry and Mineralogy of Rare Earth Elements, Reviews in Mineralogy* **21**, 169–200.

McLennan SM, Hemming S, McDaniel DK and Hanson GN (1993) Geochemical approaches to sedimentation, provenance, and tectonics. Special Papers-Geol. Soc. Am. 21–.

McLennan SM and Taylor SR (1991) Sedimentary rocks and crustal evolution: tectonic setting and secular trends. *The Journal of Geology* **99**, 1–21.

Nude PM, Kwayisi D, Taki NA, Kutu JM, Anani CY, Banoeng-Yakubo B and Asiedu DK (2015) Petrography and chemical evidence for multi-stage emplacement of western Buem volcanic rocks in the Dahomeyide orogenic belt, southeastern Ghana, West Africa. *Journal of African Earth Sciences* **112** 314–27.

Nunoo S, Hofmann A and Kramers J (2022) Geology, zircon U–Pb dating and εHf data for the Julie greenstone belt and associated rocks in NW Ghana: Implications for Birimian-to-Tarkwaian correlation and crustal evolution. *Journal of African Earth Sciences* **186**, 104444.

Osae S, Asiedu DK, Banoeng-Yakubo B, Koeberl C and Dampare SB (2006) Provenance and tectonic setting of Late Proterozoic Buem sandstones of southeastern Ghana: Evidence from geochemistry and detrital modes. *Journal of African Earth Sciences* **44**, 85–96.

Palme H and O'Neill HS. T. C (2014) Cosmochemical estimates of mantle composition. In *The Mantle and Core* (pp. 1–39). Elsevier.**Porter SM, Knoll AH and Affaton P** (2004) Chemostratigraphy of Neoproterozoic cap carbonates from the Volta basin, West Africa. *Precambrian Research* **130**, 99–112.

Potrel A, Peucat JJ and Fanning CM (1998) Archean crustal evolution of the West African Craton: example of the Amsaga Area (Reguibat Rise). U-Pb and Sm-Nd evidence for crustal growth and recycling. *Precambrian Research* **90**, 107–17.

Potter EK, Esat TM, Schellmann G, Radtke U, Lambeck K and McCulloch MT (2004) Suborbital-Period sea-level oscillations during marine isotope substages 5a and 5c. *Earth and Planetary Science Letters* **225**(1-2), 191–204.

Rudnick RL and Gao S (2003) Composition of the continental crust. *The Crust* **3**, 1–64.

Sakyi PA, Anum S, Su BX, Nude PM, Su BC, Asiedu DK, Nyame F and Kwayisi D (2018) Geochemical and Sr-Nd isotopic records of Paleoproterozoic metavolcanics and mafic intrusive rocks from the West African Craton: Evidence for petrogenesis and tectonic setting. *Geological Journal* **53**, 725–41.

Sakyi PA, Manu J, Su BX, Kwayisi D, Nude PM and Dampare SB (2019) Geochemical and Sm-Nd isotopic evidence for the composition of the Palaeoproterozoic crust of the West African Craton in Ghana. *Geological Journal* **54**, 3940–57.

Sakyi PA, Su BX, Anum S, Kwayisi D, Dampare SB, Anani CY and Nude PM (2014) New zircon U–Pb ages for erratic emplacement of 2213–2130 Ma Paleoproterozoic calc-alkaline I-type granitoid rocks in the Lawra volcanic belt of Northwestern Ghana, West Africa. *Precambrian Research* **254**, 149–68.

Sakyi PA, Su BX, Manu J, Kwayisi, D, Anani CY, Alemayehu M, Malaviarachchi SP, Nude PM and Su BC (2020) Origin and tectonic significance of the metavolcanic rocks and mafic enclaves from the Palaeoproterozoic Birimian Terrane, SE West African Craton, Ghana. *Geological Magazine* **157**, 1349–66.

Santos JO. S, Rizzotto GJ, Potter PE, McNaughton NJ, Matos RS, Hartmann LA and Quadros ME. S (2008) Age and autochthonous evolution of the Sunsás Orogen in West Amazon Craton based on mapping and U–Pb geochronology. *Precambrian Research* **165**, 120–52.

Tassinari CC. G, Bettencourt JS, Geraldes MC, Macambira MJ.B and Lafon JM (2000), The Amazon craton, In Cordani, UG, Milani, EJ, Thomaz-Filho, A and Campos, DA, eds., Tectonic evolution of South America: Rio de Janeiro, Brazil, 31st Inter. Geol. Con., 41–95.

Tassinari CC. G, Teixeira W, Nutman AP, Szabó GA, Mondin M and Sato K (2001) Archean crustal evolution of the Imataca Complex, Amazonian Craton: Sm–Nd, Rb–Sr e U–Pb (SHRIMP) evidences. Simpósio de Geologia da Amazônia, *7*.

Thiéblemont D, Goujou JC, Egal E, Cocherie A, Delor C, Lafon JM and Fanning CM (2004) Archean evolution of the Leo Rise and its Eburnean reworking. *Journal of African Earth Sciences* **39**, 97–104.

Verma SP and Armstrong-Altrin JS (2016) Geochemical discrimination of siliciclastic sediments from active and passive margin settings. *Sedimentary Geology* **332**, 1–12.

Whitney DL and Evans BW (2010) Abbreviations for names of rock-forming minerals. *American Mineralogist* **95**, 185–87.

Wright JB, Hastings DA, Jones WB and Williams HR (1985) *Geology and Mineral Resources of West Africa* (Vol. **187**). London: Allen & Unwin.

Yao J, Shu L and Santosh M (2011) Detrital zircon U–Pb geochronology, Hf-isotopes and geochemistry—new clues for the Precambrian crustal evolution of Cathaysia Block, South China. *Gondwana Research* **20**, 553–67.

https://doi.org/10.1017/S001675682400027X